NASA Contractor Report **189601**

ICASE INTERIM REPORT 20

NUMERICAL SIMULATION OF TRANSIENT HYPERVELOCITY FLOW IN AN EXPANSION TUBE

P. A. Jacobs

NASA Contract No. NAS1-18605
January 1992

INSTITUTE FOR COMPUTER APPLICATIONS IN SCIENCE AND ENGINEERING
NASA Langley Research Center, Hampton, Virginia 23665

Operated by the Universities Space Research Association

NASA
National Aeronautics and
Space Administration

Langley Research Center
Hampton, Virginia 23665-5225

ICASE INTERIM REPORTS

ICASE has introduced a new report series to be called ICASE Interim Reports. The series will complement the more familiar blue ICASE reports that have been distributed for many years. The blue reports are intended as preprints of research that has been submitted for publication in either refereed journals or conference proceedings. In general, the green Interim Report will not be submitted for publication, at least not in its printed form. It will be used for research that has reached a certain level of maturity but needs additional refinement, for technical reviews or position statements, for bibliographies, and for computer software. The Interim Reports will receive the same distribution as the ICASE Reports. They will be available upon request in the future, and they may be referenced in other publications.

M. Y. Hussaini
Chief Scientist/Acting Director

NUMERICAL SIMULATION OF TRANSIENT HYPERVELOCITY FLOW IN AN EXPANSION TUBE

P. A. Jacobs[1]
Institute for Computer Applications in Science and Engineering
NASA Langley Research Center
Hampton, VA 23665

ABSTRACT

We present several numerical simulations of the transient flow of helium in an expansion tube. The aim of the exercise is to provide further information on (and hopefully further insight into) the operational problems of the NASA Langley expansion tube. The calculations were performed with an axisymmetric Navier-Stokes code based on a finite-volume formulation and upwinding techniques. Although laminar flow and ideal bursting of the diaphragms was assumed, the simulations showed some of the important features seen in the experiments. In particular, the discontinuity in tube diameter at the primary diaphragm station introduced a transverse perturbation to the expanding driver gas and this perturbation was seen to propagate into the test gas under some flow conditions. The disturbances seen in the test flow can be characterized as either "small-amplitude" noise possibly introduced during shock compression or "large-amplitude" noise associated with the passage of the reflected head of the unsteady expansion.

[1]This research was supported by the National Aeronautics and Space Administration under NASA Contract No. NAS1-18605 while the author was in residence at the Institute for Computer Applications in Science and Engineering (ICASE), NASA Langley Research Center, Hampton, VA 23665.

Nomenclature, Units

A	: (x,y)-plane cell area
a	: local speed of sound, m/s
C_p	: coefficient of heat capacity (constant P), J/kg
C_v	: coefficient of heat capacity (constant volume), J/kg
E	: total energy (internal + kinetic), J/kg
e	: specific internal energy, J/kg
$\hat{e}$	: unit vector
F	: algebraic vector of x-component fluxes
G	: algebraic vector of y-component fluxes
h	: specific enthalpy, J/kg
k	: coefficient of thermal conductivity
$\hat{n}$	: unit normal vector
P	: pressure, Pa
Pr	: Prandtl number, $(C_p\mu/k)$
Q	: algebraic vector of source terms
q	: heat flux
R	: gas constant, $J/kg/K$
Re	: Reynolds number
r	: radial coordinate, m
T	: temperature, K
t	: time, s
U	: algebraic vector of conserved quantities
$\overline{U}$	: Riemann invariant, m/s
u	: x-component of velocity, m/s
v	: y-component of velocity, m/s
x	: x-coordinate, m
y	: y-coordinate (radial), m
β	: parameter in Mirels' boundary layer theory
ρ	: density, kg/m^3
γ	: ratio of specific heats
λ	: second coefficient of viscosity
τ	: shear stress, Pa
μ	: coefficient of viscosity, $Pa.s$
Ω	: cell volume, m^3
Ω'	: volume per radian for the axisymmetric cell
$< \bullet >$	: cell-averaged value

Subscripts

0	: conditions immediately behind the shock
1 ... 20	: gas state as shown on Fig. 1
e	: conditions just outside the boundary layer
i	: interaction of expansion with driver-gas/test-gas interface
v	: viscous contribution
w, *wall*	: wall value
x,y	: cartesian components

1 Introduction

The expansion tube is a member of the family of pulse-type aerodynamic facilities designed to provide high enthalpy test gas for short durations. It has a fundamental advantage over the reflected-shock tunnel because its operating cycle does not involve the stagnation of the heated test gas. Hence, it can provide a final test flow with low ionization and low dissociation. Initial theoretical studies of the expansion tube [1] indicated that such a machine could provide a wide range of test flows by simply altering the initial filling pressures. However, operational experience (see e.g. [2, 3]) indicated that the test flow was often contaminated by large-amplitude disturbances. The purpose of this report is to present some numerical simulations of an entire (but idealized) expansion tube in order to provide some further information (and hopefully some insight into) the mechanisms causing the disturbances in the test flow. The specific facility configuration and the flow conditions considered here are based on the experimental perfect-gas study undertaken by Shinn and Miller [3].

1.1 Facility Operation

An expansion tube is essentially a single tube divided into three sections by "primary" and "secondary" diaphragms as shown in lower part of Fig. 1 (which is reproduced from [3]). The strong primary diaphragm separates the driver tube and the intermediate (or shock) tube while the light secondary diaphragm separates the intermediate tube from the acceleration tube. The intermediate- and acceleration tubes have the same diameter. Initially, the driver tube contains a "driver gas" at high pressure (state 4) while the intermediate tube contains the test gas (state 1) and the acceleration tube contains a low pressure "acceleration gas" (state 10). The aerodynamic model to be tested is located near the downstream end of the acceleration tube.

The operation of the facility, starting with the rupture of the primary diaphragm at $t = 0$, is shown schematically in the top part of Fig. 1. The numbering of the flow states is the same as that introduced by Trimpi [1]. High pressure driver gas expands into the intermediate tube (state 3) and shock-compresses the test gas (state 2). Simultaneously an expansion fan travels upstream into the driver tube. On reaching the end of the intermediate tube, the shock ruptures the secondary diaphragm (ideally without producing disturbances) and the leading portion of the shock-compressed test gas is allowed to expand into the acceleration tube to reach the test flow conditions (state 20). The expanded test gas will have a high velocity (typically $6 - 8$ km/s) and a relatively low temperature (several hundred degrees

Kelvin).

As shown in Fig. 2, test time commences after the passage of the test-gas/acceleration-gas interface and ideally finishes with the arrival of the downstream end of the unsteady expansion (and a corresponding increase in pitot pressure). Not all of the shock-compressed test gas is expanded to the test flow state (20) and so test times are typically measured in tens to hundreds of microseconds. When the upstream-head of the unsteady expansion intersects the driver-gas/test-gas interface, a partial reflection will occur and, for some test conditions, this wave (which travels along a $u + a$ characteristic) will arrive at the end of the acceleration tube before the unsteady expansion itself. Unfortunately, ideal operation of the facility is seldom realized as test flows are typically very noisy and may have peak-to-peak variations of 50% in pitot pressure.

1.2 Previous Studies

The cause of the test flow disturbances has been the focus of several studies. Shinn and Miller [3] made experimental measurements in the NASA Langley facility using helium as both test and driver gas in order to eliminate chemical effects. They observed that most of the operating conditions resulted in test flows which were very noisy but identified an optimum condition ($P_1 = 3.45\ kPa,\ P_{10} = 16\ Pa$) with approximately 300 μs test time before the onset of large-amplitude fluctuations in the pitot pressure. A large dip in the pitot pressures was observed for values of P_{10} significantly larger than 20 Pa and this was attributed to boundary layer transition. They also identified the importance of the diaphragm dynamics on the quality of the test flow, especially at low initial pressures, but they did not identify the mechanism causing the early disturbances in the test gas.

More recently, equivalent experiments [4] using both helium and argon as the working gas were performed at the University of Queensland to check the Langley results [3] and see if the useful range of test conditions could be expanded. In conjunction with these experiments, a numerical study (based on quasi-one-dimensional modelling) was undertaken [5] to see if the test gas disturbances could be caused by "blobs" of dense driver gas being accelerated through the expanding test gas. It was concluded that, even if the blobs existed, they would not arrive early enough to cause the test-flow disturbances. However, the reflection of the unsteady expansion off the driver-gas/test-gas interface could (under some conditions) arrive early enough to introduce the noise. Test time estimates based on this mechanism are given in [6] and are consistent with the present numerical simulations.

Paull [4, 7, 8] has pursued the possibility of acoustic disturbances being generated near the primary diaphragm station and then being propagated through the unsteady expansion

of the driver gas. A family of transverse waves can exist and, when propagated through the expansion, will undergo a frequency shift such that a single dominant frequency will emerge. Transmission of these waves across the interface and into the test gas is assumed to be determined by the acoustic impedance mismatch at the interface. For situations where the sound speed in the test gas is much larger than that in the expanded driver gas, attenuation of the waves in the test gas should occur. Otherwise, a significant fraction of the noise will be transmitted. This simple rule-of-thumb does not seem to hold for the simulations presented here.

2 The Numerical Method

The computations reported here were performed with a finite-volume upwind code based on the full Navier-Stokes equations. The code is described briefly here but further detail is available in [9].

2.1 Governing Equations

For an axisymmetric flow (with y as the radial coordinate), the finite-volume formulation of the Navier-Stokes equations may be expressed as

$$\frac{d < U >}{dt} + \frac{1}{\Omega'} \int_S (yF - yF_v)\, dy - \frac{1}{\Omega'} \int_S (yG - yG_v)\, dx = Q' \tag{1}$$

where $< \bullet >$ indicates a volume average, Ω' is the volume per radian and S is a contour in the (x, y)-plane around the volume. The U, F and G vectors are

$$U = \begin{bmatrix} \rho \\ \rho u \\ \rho v \\ \rho E \end{bmatrix} , \quad yF = y \begin{bmatrix} \rho u \\ \rho u^2 + P \\ \rho vu \\ \rho Eu + Pu \end{bmatrix} , \quad yG = y \begin{bmatrix} \rho v \\ \rho uv \\ \rho v^2 + P \\ \rho Ev + Pv \end{bmatrix} . \tag{2}$$

Note that, except for the "y" premultiplying factor, they are the same as those in the planar two-dimensional situation. The viscous terms are

$$yF_v = \begin{bmatrix} 0 \\ y\tau_{xx} \\ y\tau_{xy} \\ y\tau_{xx}u + y\tau_{xy}v + yq_x \end{bmatrix} , \quad yG_v = \begin{bmatrix} 0 \\ y\tau_{yx} \\ y\tau_{yy} \\ y\tau_{yx}u + y\tau_{yy}v + yq_y \end{bmatrix} , \tag{3}$$

where

$$\tau_{xx} = 2\mu \frac{\partial u}{\partial x} + \lambda \left(\frac{\partial u}{\partial x} + \frac{\partial v}{\partial y} + \frac{v}{y} \right) , \tag{4}$$

$$\tau_{yy} = 2\mu\frac{\partial v}{\partial y} + \lambda\left(\frac{\partial u}{\partial x} + \frac{\partial v}{\partial y} + \frac{v}{y}\right) \quad , \tag{5}$$

$$\tau_{xy} = \tau_{yx} = \mu\left(\frac{\partial u}{\partial y} + \frac{\partial v}{\partial x}\right) \quad , \tag{6}$$

and

$$q_x = -k\frac{\partial T}{\partial x} \quad , \quad q_y = -k\frac{\partial T}{\partial y} \quad . \tag{7}$$

Treating the viscous contributions in the form $y\tau$ avoids any difficulties with the geometry singularity at $y = 0$. The *effective* source term is

$$Q' = \begin{bmatrix} 0 \\ 0 \\ (P - \tau_{\theta\theta})A/\Omega' \\ 0 \end{bmatrix} \quad , \text{ where } \tau_{\theta\theta} = 2\mu\frac{v}{y} + \lambda\left(\frac{\partial u}{\partial x} + \frac{\partial v}{\partial y} + \frac{v}{y}\right) \quad . \tag{8}$$

To augment these equations, we use the equation of state for a calorically perfect gas

$$P = \rho(\gamma - 1)e \quad , \tag{9}$$

with $\gamma = 1.667$ and $R = 2077\ J/kg/K$. The corresponding specific heats are $C_v = 3114\ J/kg/K$ and $C_p = 5191\ J/kg/K$. The first coefficient of viscosity is evaluated as

$$\mu = 5.023 \times 10^{-7}\ T^{0.647}\ \ Pa.s \ , \tag{10}$$

and the second coefficient is obtained from Stokes' hypothesis $\lambda = -\frac{2}{3}\mu$. Also, a constant Prandtl number of 0.67 is assumed.

2.2 Numerical Implementation

The flow domain in the (x, y)-plane is discretized as a structured mesh of quadrilateral cells with flow properties stored at the cell centres. At each time step, the inviscid-flux vectors (2) are evaluated by first applying a MUSCL interpolation scheme to obtain "left" and "right" states at the midpoints of the cell interfaces. A locally one-dimensional (approximate) Riemann solver is then applied to obtain the interface flow properties during the time step. The spatial derivatives used in the viscous flux vectors (3)-(7) are obtained at the cell vertices by applying the divergence theorem. The source term (8) is evaluated at the cell centres. The line integrals in (1) are then evaluated using the midpoint rule and the solution advanced in time.

Although a predictor-corrector time-stepping scheme was available in the code, the solutions shown in the following sections have used Euler time stepping in order to reduce the

required cpu time for each simulation. Fig. 3 shows the density contours in the shock and driver tubes at $t = 2.0\ ms$ for case 2. Except for the fine-scale features, there are few differences in the solutions for both Euler time-stepping and predictor-corrector time-stepping on the 1604×20 grid. The differences between these "coarse-grid" solutions and the solution on the (fine) 2406×30 grid are also small. The limit on the number of cells was set by the memory available on the SUN workstations (64 *Mbytes*) and the desire to fit the jobs within the 8 *Mword* queues on the Cray-YMP (Sabre).

3 Simulation Results

Figure 4 shows the flow domain considered in the simulations. The flow is considered to be axially symmetric with the flow domain extending radially from the axis to the tube wall and axially from the closed end of the driver tube to the end of the acceleration tube where it enters the test section of the facility. Dimensions are shown in the figure. The grid was generated in three pieces, one for each section of the facility. Note that the number of cells and the clustering toward the tube wall was kept constant along the length of the domain. Also, the cell size remained constant in the axial direction. The radial distance from the outermost cell-centres to the intermediate- and acceleration-tube walls is $3.87 \times 10^{-4}\ m$.

Note that, while the change in tube radius at the primary diaphragm station is included, neither the diaphragm nor the square transition section downstream of this point is modelled. Instead, the simulations start with high-pressure reservoir conditions upstream of the primary diaphragm station and intermediate-tube initial conditions downstream of the same station (and into the acceleration tube). The simulations are allowed to proceed until the primary shock reaches the secondary diaphragm station and, at that point in time, the conditions downstream of the secondary diaphragm are reset to acceleration-tube initial conditions. Thus, the bursting of the diaphragms is considered to be ideal in the following calculations. This is in contrast to the experimental observation that the flow quality is very sensitive to rupture behaviour of the diaphragms [2, 3].

3.1 Initial State

All of the simulations used the nominal driver tube conditions discussed in [3]. These are

$$P_4 = 33\ MPa,\ \ u_4 = 0,\ \ T_4 = 330\ K,\ \ \rho_4 = 48.15\ kg/m^3,\ \ e_4 = 1.028\ MJ/kg.$$

As discussed in [3] the nominal driver-tube temperature may be lower than the actual gas temperature at primary-diaphragm rupture where a maximum value of $T_4 = 390\ K$ was

estimated. The test gas and acceleration initial conditions are

$$T_{10} = T_1 = 300\ K, \quad e_{10} = e_1 = 0.934\ MJ/kg, \quad u_{10} = u_1 = 0,$$

with pressures and densities as specified in Table 1.

For cases 1a and 1b, the conditions were chosen to approximate the optimum conditions identified in the experiment [3] and two different grids were used to check for sensitivity to grid resolution. Cases either side of this optimum condition were then considered. Case 2 has a higher intermediate-tube pressure where large-amplitude noise was observed at an earlier time in the experiment. Case 3, with a low intermediate-tube pressure, also was observed to have a noisy test flow early in the test time. Finally, case 4 considers the condition with high acceleration-tube pressure where (for the Langley expansion tube) a large dip in pitot pressure was observed shortly after the arrival of test flow [3].

3.2 Case 1: $P_1 = 3.45\ kPa$, $P_{10} = 16\ Pa$

This condition was chosen to be the starting point for the study because it was identified as the best operating condition in [3]. The experimentally observed test time was approximately 300 μs before large-amplitude noise contaminated the test flow.

Each case was run as a sequence of two hour jobs on the Cray-YMP with the flow data being written every 0.5 ms (simulation time) for the shock-compression process and every 0.1 ms for the test-gas expansion. Table 2 shows the required computer resources together with the name of the mass-store directory where the data files have been archived.

Two calculations were performed. Case 1a used a "coarse" grid of 1604 cells axially by 20 cells radially while case 1b used a "fine" grid of 2406 $\times$ 30 cells. (Refer to Appendix A for the coarse grid results.) The computed results, including the timing of events such as the passage of the shock and contact surfaces, were largely the same. There were, however, some differences in the details of the contact surfaces and the noise introduced to the test flow.

Figure 5 summarizes the calculation for case 1b as a wave diagram. The data points plotted were obtained from the individual plots of the density field shown later. Note the small size of the slug of compressed acceleration gas (state 20). The position of the long dashed line denoting the downstream-tail of the unsteady expansion of the test gas was estimated by its arrival at $x = 24\ m$ while the short-dashed line represents the propagation of the leading edge of the reflected expansion and the asterisk denotes the arrival of large-amplitude noise at the end of the acceleration tube ($x \simeq 24\ m$). This reflected expansion is

the result of the interaction between the upstream-head of the unsteady expansion and the test-gas/driver-gas interface. The test time (state 5) for this case starts after the passage of the test-gas/acceleration-gas interface and stops with the arrival of the downstream tail of unsteady expansion.

3.2.1 Shock Compression of the Test Gas

Density contours for the shock compression of the test gas are shown in Fig. 6. For each frame, 81 contours have been plotted over the range $-6.0 < \log_{10} \rho < 2.0$. Although the shock has remained essentially planar, the driver-gas/test-gas interface has become quite distorted by $t = 2.0\ ms$. Boundary layer effects are present (as can be seen by the contact surface being left behind along the tube wall) but viscous effects are not well resolved in this part of the calculation.

Of special interest is the train of transverse waves following the interface. These transverse waves show up clearly in the contours of the radial velocity as shown in Fig. 7 where it appears that the disturbances are introduced at the primary diaphragm station. Note that the axial scale is highly compressed and the actual Mach angles are much shallower than those that appear in the figure. Significant noise is present in the shocked test gas.

Figure 8 shows the axial variation of flow properties at $t = 1.0\ ms$ together with the estimated properties for a purely one-dimensional situation. Except for some noise, the levels are in general agreement. Although the axisymmetric simulation exhibits a higher shock speed than the one-dimensional case, tables 3 and 4 show that the computed shock speed is still lower than that measured in the experiment. This effect was discussed in [3] and may be partly due to a low estimate for the initial driver-gas temperature. Also, note the variation in shock speed over this phase of the facility operation (see table 4).

3.2.2 Unsteady Expansion of the Test Gas

The unsteady expansion of the test gas is shown in Fig. 9. Viscous effects are more important in this process and a very thick boundary layer is established behind the shock and test-gas/acceleration-gas interface. The separation distance of the shock and contact remains essentially constant from $t = 2.5\ ms$ to $t = 4.0\ ms$ because a balance has been reached between the mass flow of acceleration gas entering through the shock and the mass flow into the boundary layer [10]. This hot acceleration gas tends to accumulate just upstream of the test-gas/acceleration-gas interface and form a large bulge in the boundary layer (at $x \simeq 23\ m, t = 4.5\ ms$). It is not until the last frame ($t = 5.0\ ms$) that any significant level of noise is evident in the expanding test gas.

Figure 10 shows the axial variation of flow properties at $t = 4.4\ ms$. There are very obvious disturbances in the region of the expanded driver gas (state 3) and, on close inspection of the pressure distribution, some small-amplitude disturbances can be seen near the downstream end of the unsteady expansion of the test gas (at $x \simeq 22\ m$). The very high temperature of the shocked acceleration gas is interesting.

Figures 11, 12 and 13 show details of the shock and test-gas/acceleration-gas interface region. The bulge seen very clearly at $x \simeq 23\ m$, $t = 4.5\ ms$ in Fig. 9 is no longer as obvious in these "true-shape" plots. Plotting the velocity field in a frame of reference which is stationary with respect to the shock and contact surface clearly shows the bleeding of shocked acceleration gas out of region 20 and into the boundary layer. Estimates of the separation distance between the shock and contact surface (i.e. the length of region 20) can be made using the theory presented in [10]. Using the expression

$$L_{20} = \frac{r_w^2}{4\beta^2}\left(\frac{\rho_{e,0}}{\rho_{w,0}}\right)^2 \frac{u_{e,0}}{u_w - u_{e,0}} \frac{u_{e,0}\ \rho_{w,0}}{\mu_{w,0}} \tag{11}$$

together with the parameter estimates

$$\beta = 2.12, \quad u_w = U_{s,10} = 5900\ m/s, \quad u_{e,0} = 1200\ m/s,$$

$$\rho_{e,0} = 1.0 \times 10^{-4}\ kg/m^3, \quad \rho_{w,0} = 2.484 \times 10^{-4}\ kg/m^3, \quad \mu_{w,0} = 2.012 \times 10^{-5}\ Pa.s,$$

a separation length of $0.2\ m$ is obtained. This is in reasonable agreement with the length observed in Fig. 11 but it should be noted that the value of L_{20} obtained from eqn. (11) is very sensitive to the estimated parameters.

3.2.3 Histories of the Test Flow Properties

Histories of the centreline test-flow properties near the exit of the acceleration tube are shown in Fig. 14. Features that can be identified include the passage of the shock and the test-gas/acceleration-gas interface at times $t = 4.45\ ms$ and $t = 4.83\ ms$ respectively. These events are followed by a gradual variation in properties possibly due to a constriction of the effective tube diameter associated with the passage of the bulge (identified in Fig. 9). The downstream tail of the unsteady expansion arrives at $t = 4.63\ ms$ and average pressure and density begin to rise while Mach number and velocity decline. It is in the period $4.6 < t < 5.0$ that a "low-amplitude" fluctuation is evident.

The fluctuations increase in both the amplitude and the frequency with the arrival of the reflected head of the unsteady expansion at $t = 5.04\ ms$. This wave originates with the rupture of the secondary diaphragm and travels along a $u_2 - a_2$ characteristic until it strikes

the driver-gas/test-gas interface. There is both transmission into the driver gas and partial reflection downstream along a $u + a$ characteristic thus admitting more disturbances into the expanding test gas. The arrival time for this wave (at the exit plane of the acceleration tube) may be estimated as described in [6]. We start at $x' = 0,\ t' = 0$ with the rupture of the secondary diaphragm. The upstream head of the unsteady expansion intersects the driver-gas/test-gas interface at $t' = \Delta t_i,\ x' = (u_2 - a_2)\ \Delta t_i$. Refer to tables 5 and 6 for particular values. The propagation time of the wave through the unsteady expansion may be obtained by integration along a $u + a$ characteristic for which the Riemann invariant is [11]

$$u_5 + \frac{2}{\gamma - 1} a_5 = \overline{U} = u + \frac{2}{\gamma - 1} a \quad . \tag{12}$$

Within the centred expansion we have

$$\frac{x'}{t'} = u - a \quad , \tag{13}$$

and this may be substituted into equation (12) to obtain

$$\begin{aligned} a &= \frac{\gamma - 1}{\gamma + 1} \left(\overline{U} - \frac{x'}{t'} \right) \quad , \\ u &= \frac{\gamma - 1}{\gamma + 1} \left(\overline{U} + \frac{2}{\gamma - 1} \frac{x'}{t'} \right) \quad . \end{aligned} \tag{14}$$

The integration may be terminated at the end of the expansion ($a = a_5$) or at the end of the acceleration tube, whichever is sooner. If the reflected wave reaches the downstream end of the expansion before it reaches the end of the tube, it continues to propagate into the test flow region (20) with speed $u_5 + a_5$. The time of arrival as computed with this approach closely matches the onset of large-amplitude noise in the exit flow histories.

A comparison of computed test flow properties with the measurements of Shinn and Miller [3] is shown in Fig. 15. The overall level of the computed wall pressure is a little low, possibly because of the low estimate for the initial temperature in the driver tube. Also, the computed wall pressure is smoother than the experimental wall pressure but this may be partly due to numerical dissipation and partly due to noisy measurement techniques in the experiment. The good news is that arrival of the downstream tail of the unsteady expansion (0.2 ms after the shock) agrees well.

The other frames in Fig. 15 show pitot pressures. The computed pitot pressure at the centreline is again a little lower than the experimental value and is also less noisy for the first 0.4 ms after shock arrival. However, there is good agreement in that there appear to be two types of noise: a small-amplitude noise before the arrival of the reflected head of the

unsteady expansion and a large-amplitude noise after the passage of the reflected expansion. This is one of the main results of this study.

Other features evident in the pitot histories include the large dip at $t = 5.0\ ms$, $r = 52.5\ mm$ and the consistently low values at $r = 71\ mm$. The large dip is associated with the passage of the bulge in the boundary layer while the $r = 71\ mm$ position remains within the boundary layer after the passage of the test-gas/acceleration-gas interface.

3.3 Case 2: $P_1 = 20.62\ kPa$, $P_{10} = 16\ Pa$

Having successfully simulated the arrival of noise in the test flow at $P_1 = 3.45\ kPa$, we decided to try a higher pressure of $P_1 = 20.62\ kPa$ where the experimental measurements indicated that large-amplitude disturbances appear very early in the test flow. Fig. 16 shows the wave diagram for this case. Note that the downstream tail of the unsteady expansion arrives at the tube exit shortly after the test flow begins and that the reflected head of the unsteady expansion is expected to arrive much later.

The shock compression of the test gas is shown in Fig. 17. Because of the higher initial intermediate-tube pressure, the shock has a lower speed than in case 1. Transverse waves are still present in the expanded driver gas but they seem to be weaker. Also, there is some noise in the compressed test gas.

The unsteady expansion of the test gas is shown if Fig. 18. The process appears similar to that in case 1 except that there is very little noise evident in the expanded test gas (even at $t = 5.0\ ms$). This lack of noise is confirmed in Fig. 19 and Fig. 20. In Fig. 20, the arrival of the downstream-tail of the unsteady expansion can be clearly seen at $t \simeq 4.8\ ms$ while the reflected head of the unsteady expansion is not expected to arrive at the tube exit until $t \simeq 5.84\ ms$ (see table 6).

Fig. 21 compares the computed pressures at the exit of the acceleration tube with experimental measurements. The lack of noise in the laminar solution suggests that the disturbances in the experimental test flow are caused by boundary layer transition or turbulence (which is not modelled in these simulations) rather than propagation of noise through the driver-gas/test-gas interface.

3.4 Case 3: $P_1 = 1.74\ kPa$, $P_{10} = 16\ Pa$

Given the failure of the $P_1 = 20.62\ kPa$ case to exhibit large disturbances in the simulated test flow, we decided to try a case with lower intermediate-tube pressure than case 1. Figures 22 - 27 show the results of a simulation with $P_1 = 1.74\ kPa$, $P_{10} = 16\ Pa$.

Table 4 shows that the shock speed during the initial compression of the test gas is slightly higher than for case 1 but that the final shock speed during the unsteady expansion process is slightly lower. The shock compression of the test gas (Fig. 23) appears to be noisier than for case 1 and the centreline histories (Fig. 26) indicate that small-amplitude disturbances appear very early in the test flow. This seems to be consistent with the experimental pitot pressure results shown in Fig. 27. The arrival of the reflected head of the unsteady expansion ($t \simeq 5.1\ ms$) can be seen as a decrease in the growth rate of pitot pressure and, in the simulation, is accompanied by larger-amplitude and higher-frequency disturbances which are not obvious in the experimental measurements.

3.5 Case 4: $P_1 = 3.45\ kPa$, $P_{10} = 52.6\ Pa$

For large values of acceleration-tube filling pressures, Shinn and Miller [3] also observed a large dip in the pitot pressure shortly after the start of the test flow. The phenomenon was attributed to boundary layer transition. We decided to try simulating such an operating condition to see if the bulge in the boundary layer (following the test-gas/acceleration-gas contact surface) was a contributing factor.

The results for the laminar-flow simulation with $P_1 = 3.45\ kPa$, $P_{10} = 52.6\ Pa$ are shown in figures 28 - 32. The shock compression phase is the same as for case 1a but, with the larger mass of acceleration gas, the separation distance between the shock and the contact surface is increased and equilibrium is attained by $t = 2.8\ ms$. The histories of the centreline properties shown in Fig. 31 indicate that small-amplitude noise is present in both the acceleration gas and test gas up until the arrival of the reflected head of the unsteady expansion at $t \simeq 4.9\ ms$. Although the large-amplitude noise after the passage of the reflected expansion seems to be consistent with the experimental measurements shown in Fig. 32, there is no evidence of the large pitot-pressure dip in the laminar simulation. This is consistent with the hypothesis [3] that the dip is caused by boundary layer transition. Note that this case was computed on a coarse mesh which may result in the attenuation of the high-frequency components of the noise (see appendix A).

4 Concluding Remarks

From the computational point of view, we can now make reliable simulations for laminar axisymmetric flow of a perfect gas in an expansion tube. Viscous effects were adequately resolved in the acceleration tube but they were not well resolved in either the intermediate tube

or the driver tube. This is not considered to be a major problem as inviscid multidimensional flow features seem to dominate the performance of these sections of the facility.

The numerical technique is capable of capturing strong shocks and contact surfaces with large temperature jumps, however the contact surfaces tend to be more (numerically) smeared than the shocks. The net result is that the estimates of wave propagation times and test flow properties appear to be in reasonable agreement with experimental measurements. However, the issue of reliably capturing the high-frequency noise is not fully settled and further computational experiments using alternative higher-order schemes (such as ENO [12]) are required.

We deliberately selected a laminar perfect-gas flow to keep this study manageable but there is an immediate need to perform simulations with nonideal thermal and chemical effects with turbulence in three-dimensions. Diaphragm dynamics is another important item which needs to be considered for future study. In the near future, it is unlikely that we could include all of these features but the modelling of turbulence and the diaphragm dynamics are key items required to simulate the expansion tube over a larger range of useful operating conditions.

With respect to facility design and operation, the simulations show some important features. Firstly, the discontinuity at the primary diaphragm station is sufficient to produce disturbances which may then propagate into the test flow. Secondly, the simulations identify two categories of noise in the test flow. One is a small-amplitude disturbance which may be seen before the arrival of the reflected head of the unsteady expansion while the other is a large-amplitude noise associated with the passage of the reflected expansion.

This distinction explains the experimental observation [4, 5] that increasing the acceleration-tube pressure P_{10} while keeping the intermediate-tube pressure P_1 constant results in higher frequency noise in the test flow. The increase in P_{10} results in a lower shock speed in the acceleration tube, while the fixed P_1 means that the arrival time of the reflected expansion will be essentially constant. Thus, at high values of P_{10}, we expect the reflected expansion to arrive very soon after the shock and introduce high-frequency disturbances to the test flow.

To avoid the large-amplitude noise, it should be relatively simple to select operating conditions or facility configurations which delay the arrival of the reflected expansion. For example, the intermediate tube could be lengthened while fixing the initial gas pressures.

It is not immediately obvious how to avoid the small-amplitude disturbances observed before the arrival of the unsteady expansion. As can be seen in Fig. 33 these disturbances do not appear in the test flow for all operating conditions. It was hoped that the acoustic theory

of Paull would provide some guide to the correct selection of good operating conditions. The basic result of that theory is that noise crossing the driver-gas/test-gas interface is attenuated if the speed of sound in the test gas is much higher than the speed of sound in the driver gas. This jump in sound speeds is present for each of the cases studied here but, in contrast to Paull's theory, the case with the least noise also had the smallest jump in sound speed across the driver-gas/test-gas interface (see table 5). We suggest that a number of other operating conditions be simulated before drawing any firm conclusions.

References

[1] R. L. Trimpi. A preliminary theoretical study of the expansion tube, a new device for producing high-enthalpy short-duration hypersonic gas flows. NASA Technical Report R-133, 1962.

[2] C. G. Miller. Operational experience in the Langley expansion tube with various test gases. NASA Technical Memorandum 78637, 1977.

[3] J. L. Shinn and C. G. Miller. Experimental perfect-gas study of expansion-tube flow characteristics. NASA Technical Paper 1317, 1978.

[4] A. Paull, R. J. Stalker, and I. Stringer. Experiments on an expansion tube with a free-piston driver. AIAA Paper 88-2018, 1988.

[5] C. M. Gourlay. Expansion tube test time predictions. NASP Contractor Report 1024, 1988.

[6] A. Paull and R. J. Stalker. Theoretical and experimental test times available in an expansion tube. In *10th Australasian Fluid Mechanics Conference*, pages 12.29–12.32, 1989.

[7] A. Paull and R. J. Stalker. The effect on an acoustic wave as it traverses an unsteady expansion. *The Physics of Fluids (A)*, 3(4):717–719, 1991.

[8] A. Paull and R. J. Stalker. Acoustic waves in shock tunnels and expansion tubes. In *18th International Symposium on Shock Waves*, 1991.

[9] P. A. Jacobs. Single-block Navier-Stokes integrator. ICASE Interim Report 18, 1991.

[10] H. Mirels. Test time in low-pressure shock tubes. *The Physics of Fluids*, 6(9):1201–1214, 1963.

[11] J. D. Anderson. *Modern Compressible Flow: with Historical Perspective.* McGraw-Hill, New York, 1982.

[12] J. Casper. Finite-volume application of high-order ENO schemes to two-dimensional boundary-value problems. AIAA Paper 91-0631, 1991.

Appendix A

Coarse Grid Calculation, Case 1a.

In order to partially address the issue of grid sensitivity, we simulated the $P_1 = 3.45\ kPa$, $P_{10} = 16\ Pa$ condition on a coarse (1604×20) grid. This case is labelled 1a in tables 1 - 3. The results are shown in figures 34 - 37. Except for fine-scale detail, the results are essentially the same as for the 2406×30 (fine) grid simulation. The most notable difference is shown in Fig. 37 which compares the test flow pressures at the exit of the acceleration tube. The coarse grid has attenuated the small-amplitude noise seen before the arrival of the reflected head of the unsteady expansion and has filtered out most of the high-frequency component of the noise after the passage of the reflected expansion (at $t \simeq 5.0\ ms$). The (relative) timing of events and the mean levels of the pressures are unchanged but there is a slight time shift in the plots in order to offset a timing mistake in resetting the acceleration tube initial conditions.

Case	P_1 (kPa)	ρ_1 (kg/m^3)	P_{10} (Pa)	ρ_{10} (kg/m^3)
1a	3.45	5.537×10^{-3}	16	2.568×10^{-5}
1b	3.45	5.537×10^{-3}	16	2.568×10^{-5}
2	20.62	3.309×10^{-2}	16	2.568×10^{-5}
3	1.74	2.792×10^{-3}	16	2.568×10^{-5}
4	3.45	5.537×10^{-3}	52.6	8.442×10^{-5}

Table 1: Initial States.

Case	CFL	$cpu - time$ (hrs)	memory $(Mwords)$	t_{final} (ms)	grid	mass-store directory
1a	0.5	12.5	3.2	5.4	1604×20	exp-D2
1b	0.5-0.6	42	6.8	5.4	2406×30	exp-B
2	0.5-0.6	41.6	6.8	5.3	2406×30	exp-C
3	0.5	49	6.8	5.4	2406×30	exp-F
4	0.5	6.5	3.2	5.4	1604×20	exp-G

Table 2: Computational resources.

Case	$U_{s,1}$ (m/s)	$U_{s,10}$ (m/s)	P_5 (kPa)	$P_{5,pitot}$ (kPa)	experimental run numbers
1a,1b	4111	6914	1.00	58.8	14,134-142
2	3375	6625	1.01	122.9	31
3	4203	6840	-	-	24
4	4106	6100	2613	74.7	23

Table 3: Experimentally measured shock speeds and pressures from Shinn and Miller (1978).

Case	$U_{s,1}$ (m/s)	$U_{s,10}$ (m/s)	P_5 (kPa)	$P_{5,pitot}$ (kPa)
1b	3745, 3374	6820, 5968	0.867	51.7
2	3108	6160	1.067	127.5
3	3711	5645	0.713	33.0
4	3490	5570	0.733	72.0

Table 4: Computed shock speeds and pressures.

Case	t_{sample} (ms)	a_2 (m/s)	a_5 (m/s)	u_2 (m/s)	u_5 (m/s)	a_3 (m/s)	a_2/a_3
1b	4.4	1585	903	3351	6216	289	5.49
2	4.6	1594	616	2721	6318	345	4.62
3	4.4	1596	1037	3567	6068	251	6.37
4	4.5	1620	1122	3345	5443	281	5.75

Table 5: Flow properties across the unsteady expansion of the test gas.

Case	$t_{rupture}$ (ms)	Δt_i (ms)	$\Delta t_{propagate}$ (ms)	$t_{arrival}$ (ms)
1b	2.08	1.00	2.96	5.04
2	2.40	1.15	3.44	5.84
3	2.00	0.95	2.82	4.82
4	2.08	0.95	2.95	5.03

Table 6: Event times associated with the reflection of the unsteady expansion.

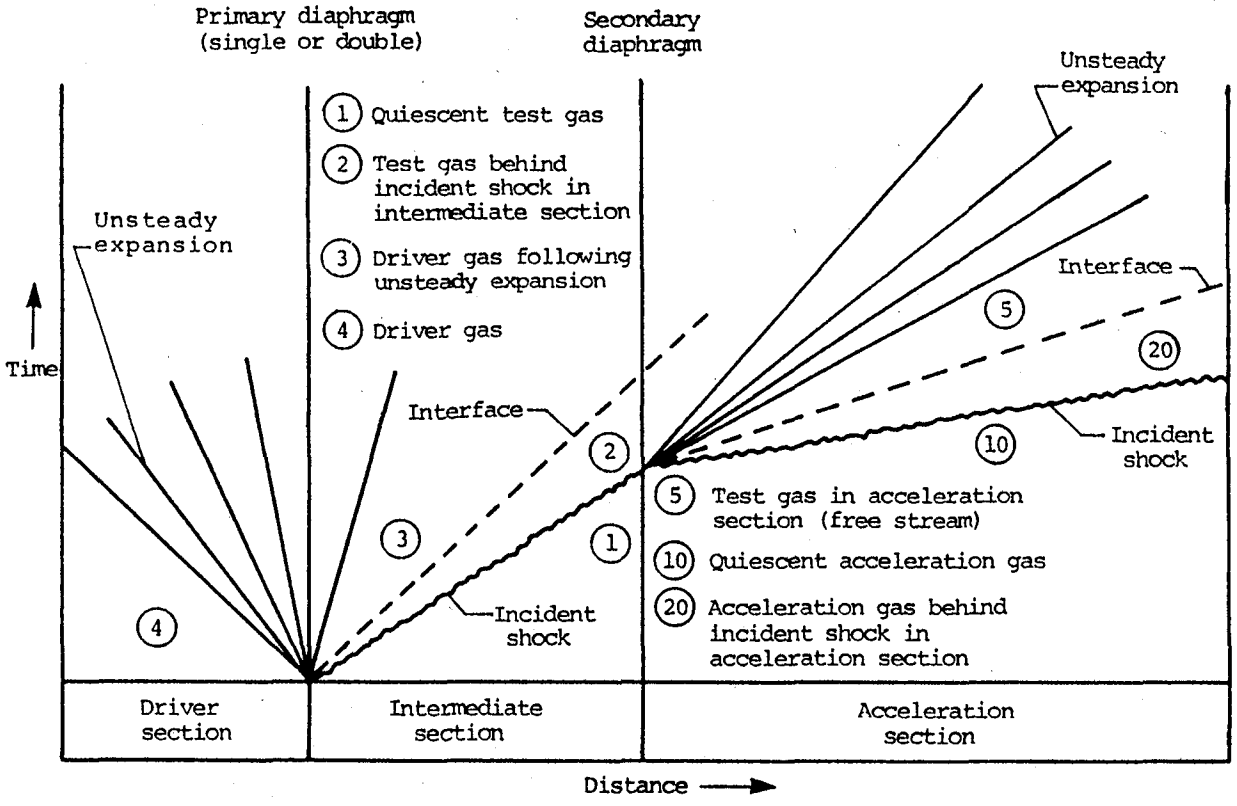

Figure 1: Conceptual wave diagram for the operation of the NASA Langley expansion tube. The numbers refer to the states of the gases as defined by Trimpi (1962).

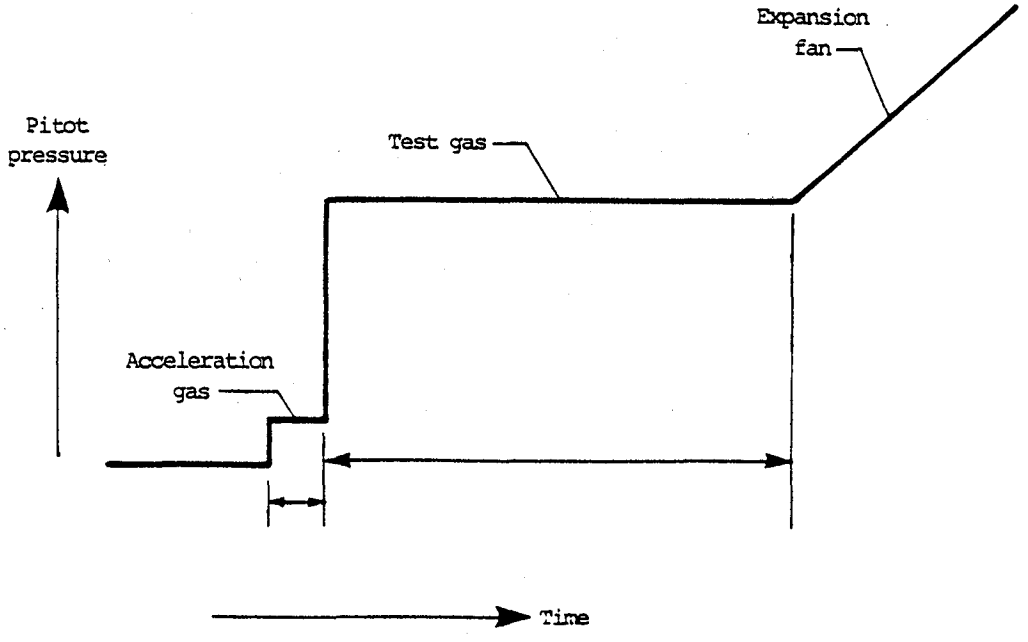

Figure 2: Ideal pitot pressure history at the exit plane of the acceleration tube.

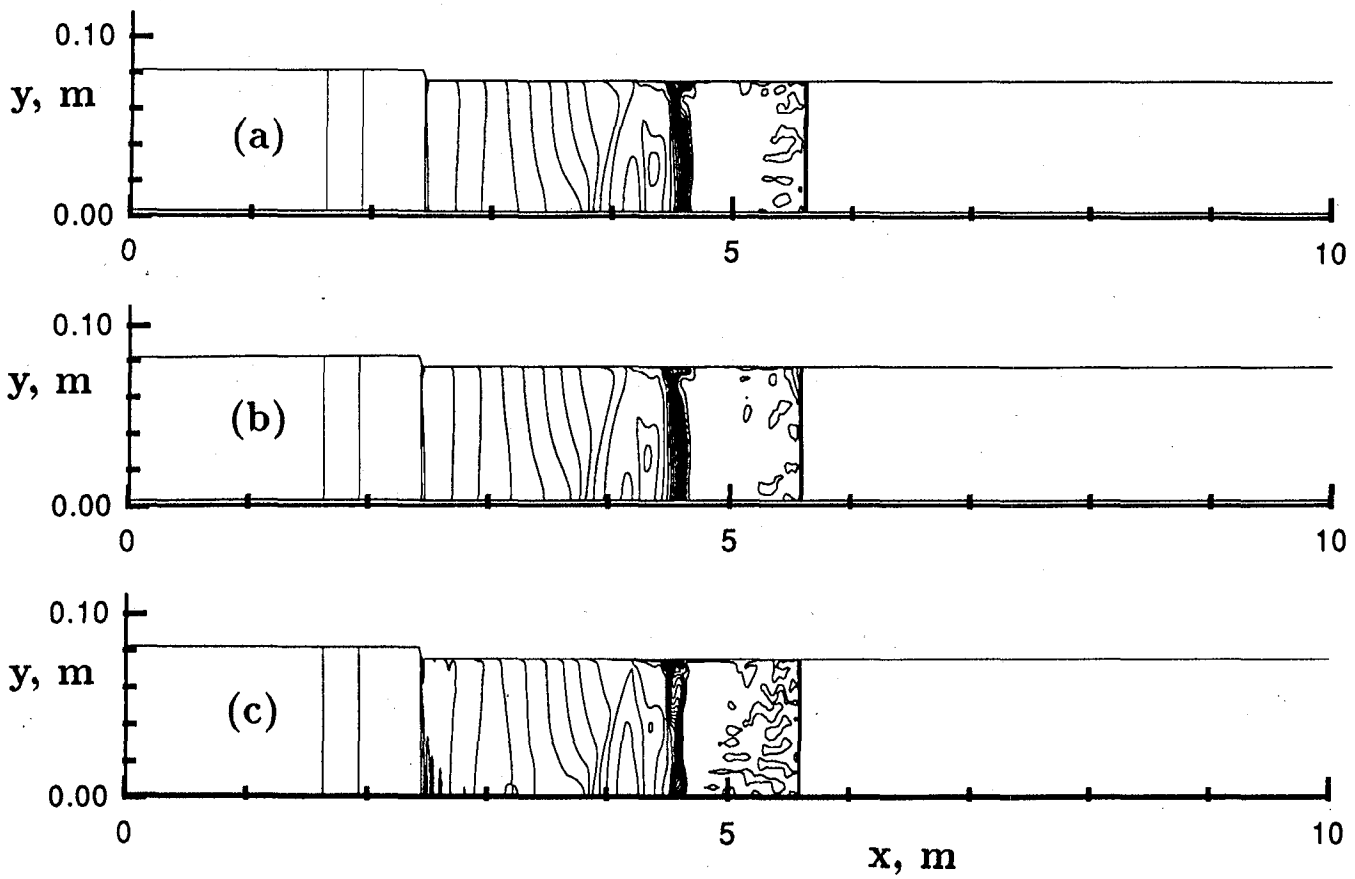

Figure 3: Comparison of the density fields at $t = 2.0\ ms$ for case 2: (a) 1604×20 grid, Euler time-stepping; (b) 1604×20 grid, predictor-corrector time-stepping; (c) 2406×30 grid, Euler time-stepping.

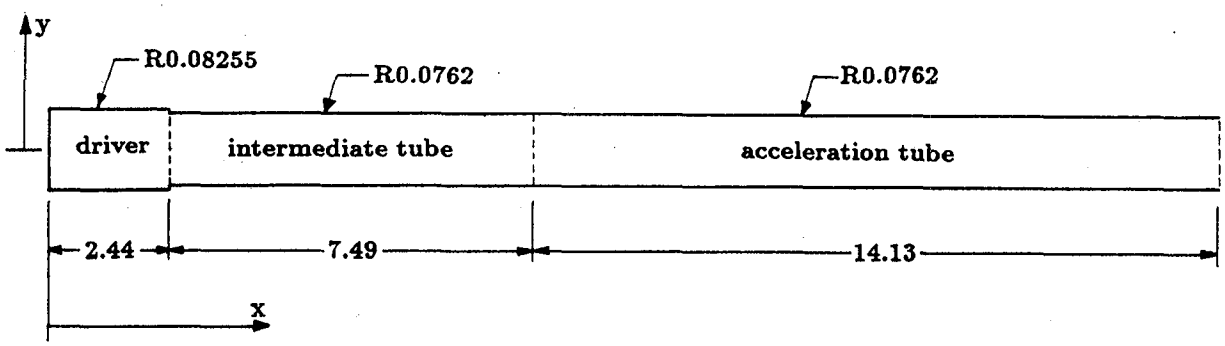

Figure 4: Expansion tube geometry as modelled in the simulations. Dimensions are in metres.

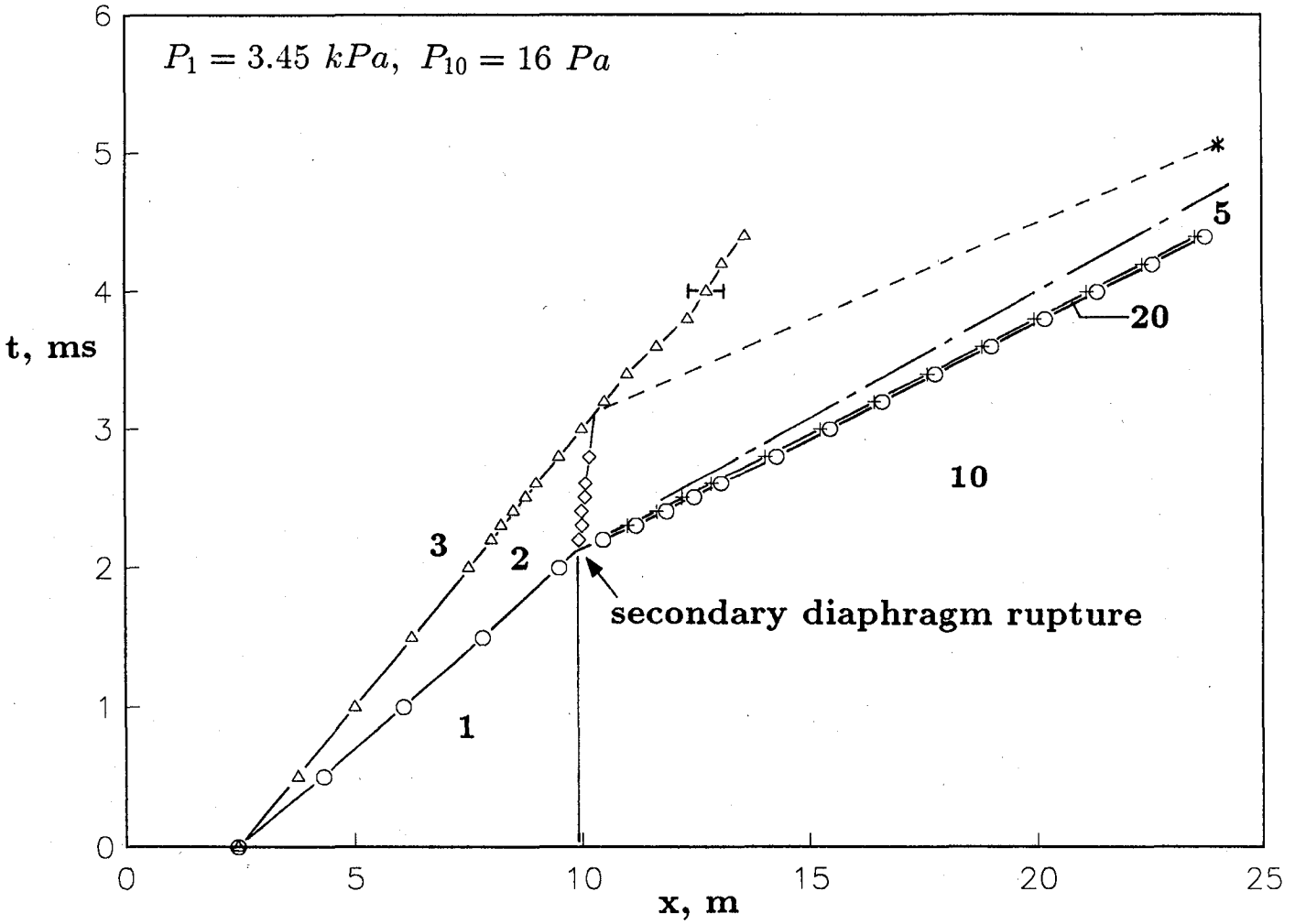

Figure 5: Wave diagram for case 1. ○ = shock; △ = driver-gas/test-gas interface; + = test-gas/acceleration-gas interface; long dash = downstream tail of the unsteady expansion; ◇ = upstream head of the unsteady expansion; short dash = reflected expansion.

$$P_1 = 3.45\ kPa,\ P_{10} = 16\ Pa$$

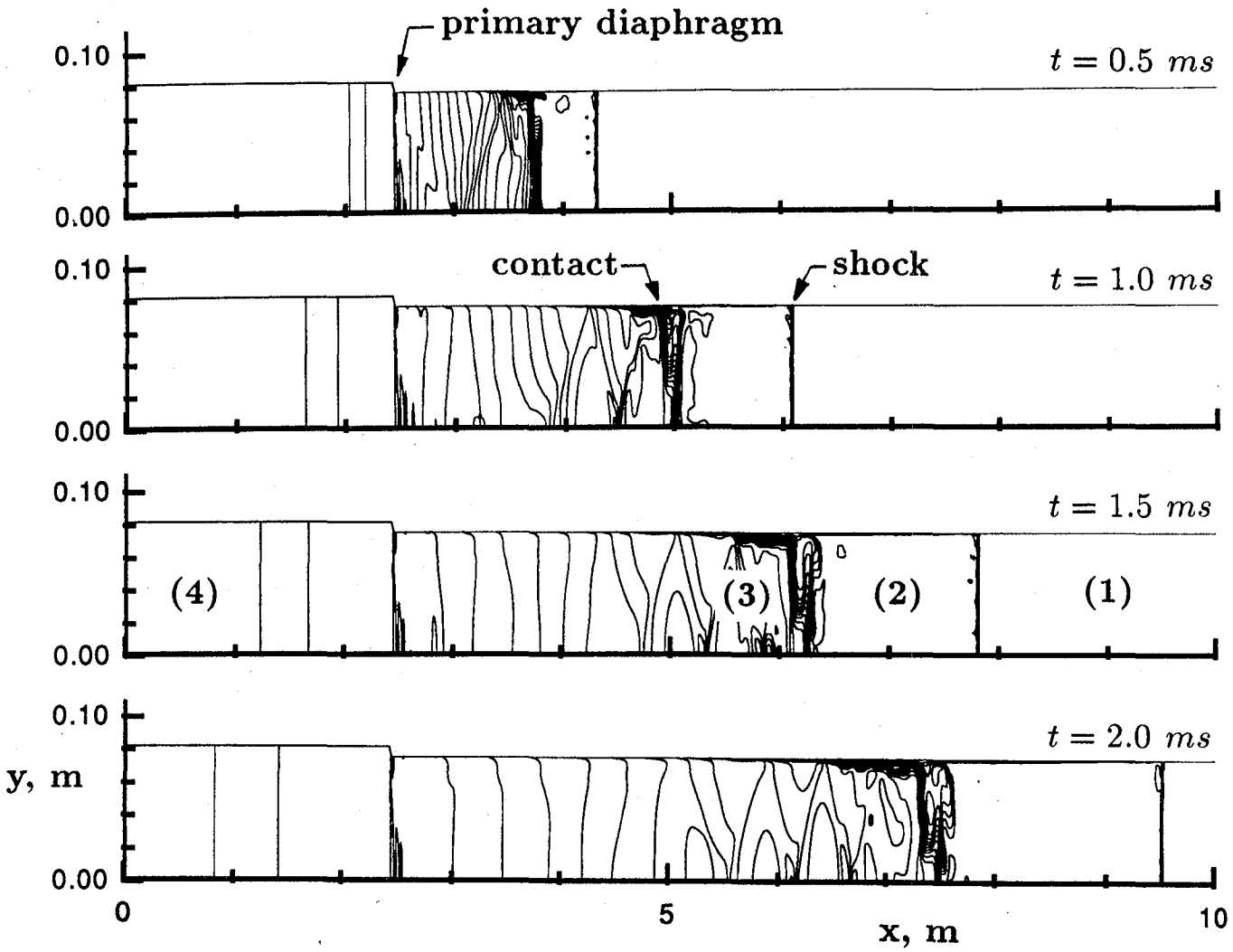

Figure 6: Density contours showing the shock compression of the test gas for case 1. The flow states are labelled as per Fig. 1.

$P_1 = 3.45\ kPa,\ P_{10} = 16\ Pa$

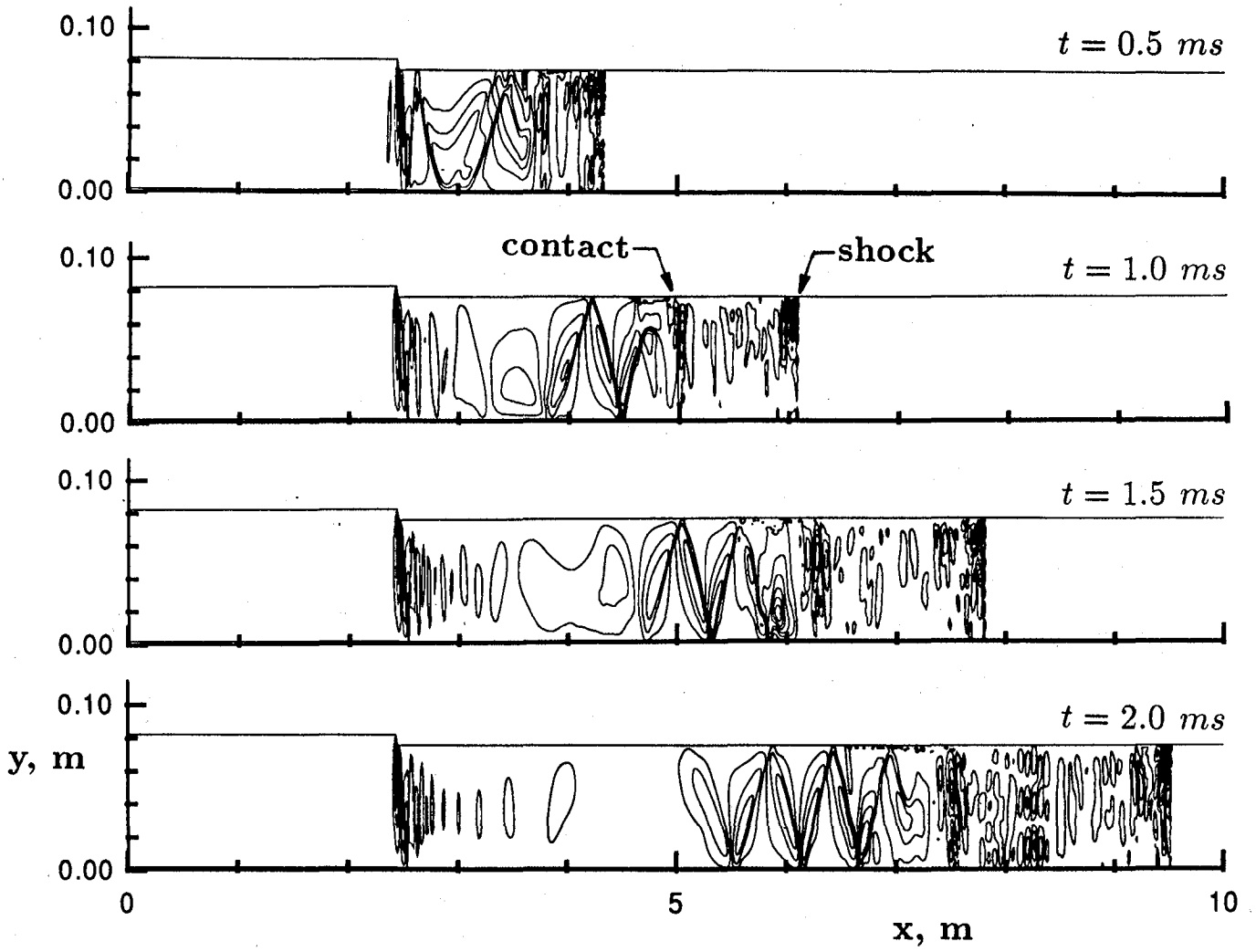

Figure 7: Transverse velocity contours for case 1.

$$P_1 = 3.45\ kPa,\ P_{10} = 16\ Pa$$

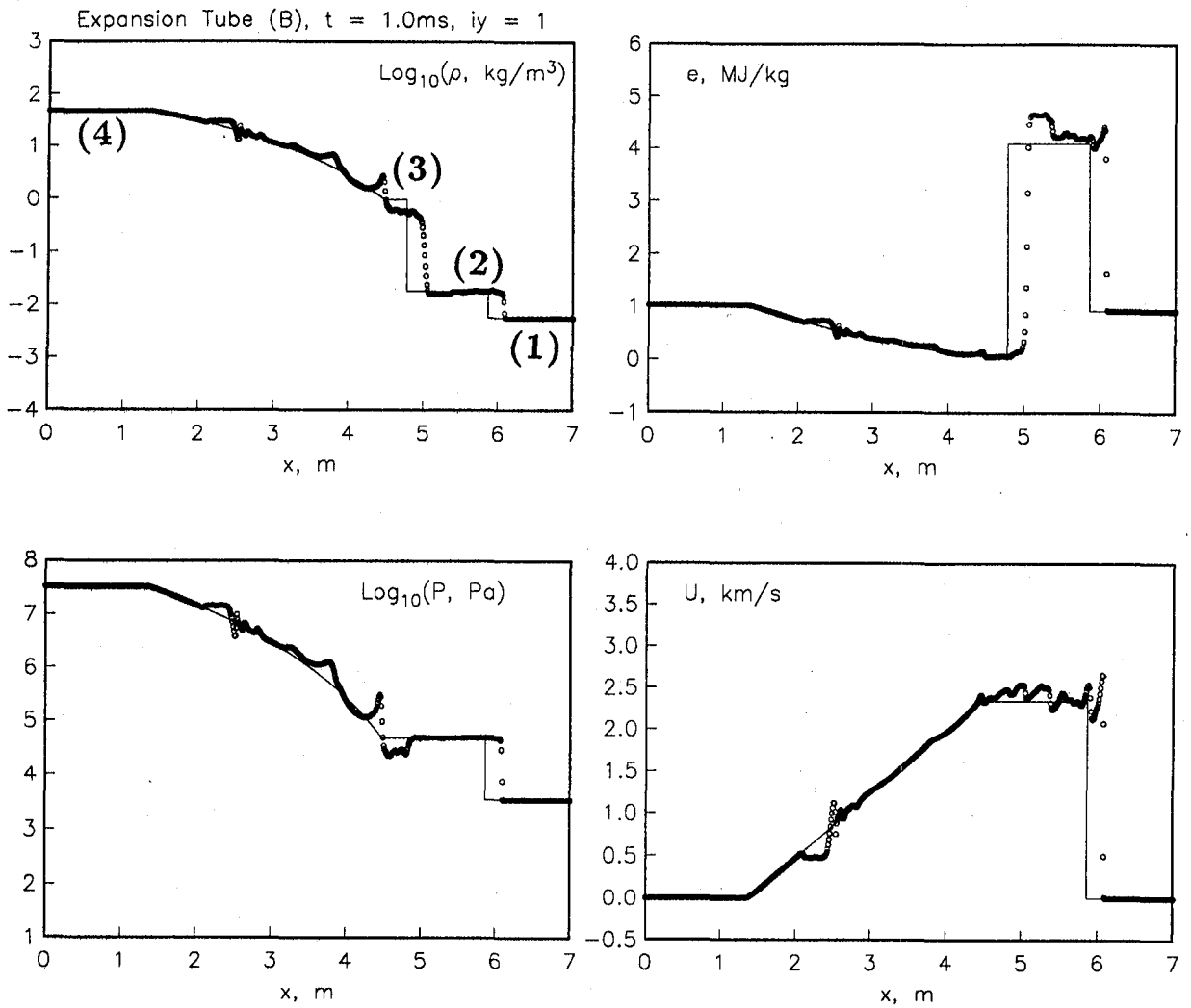

Figure 8: Flow properties along the axis during shock compression (case 1, $t = 1.0\ ms$). The solid line denotes the ideal one-dimensional solution.

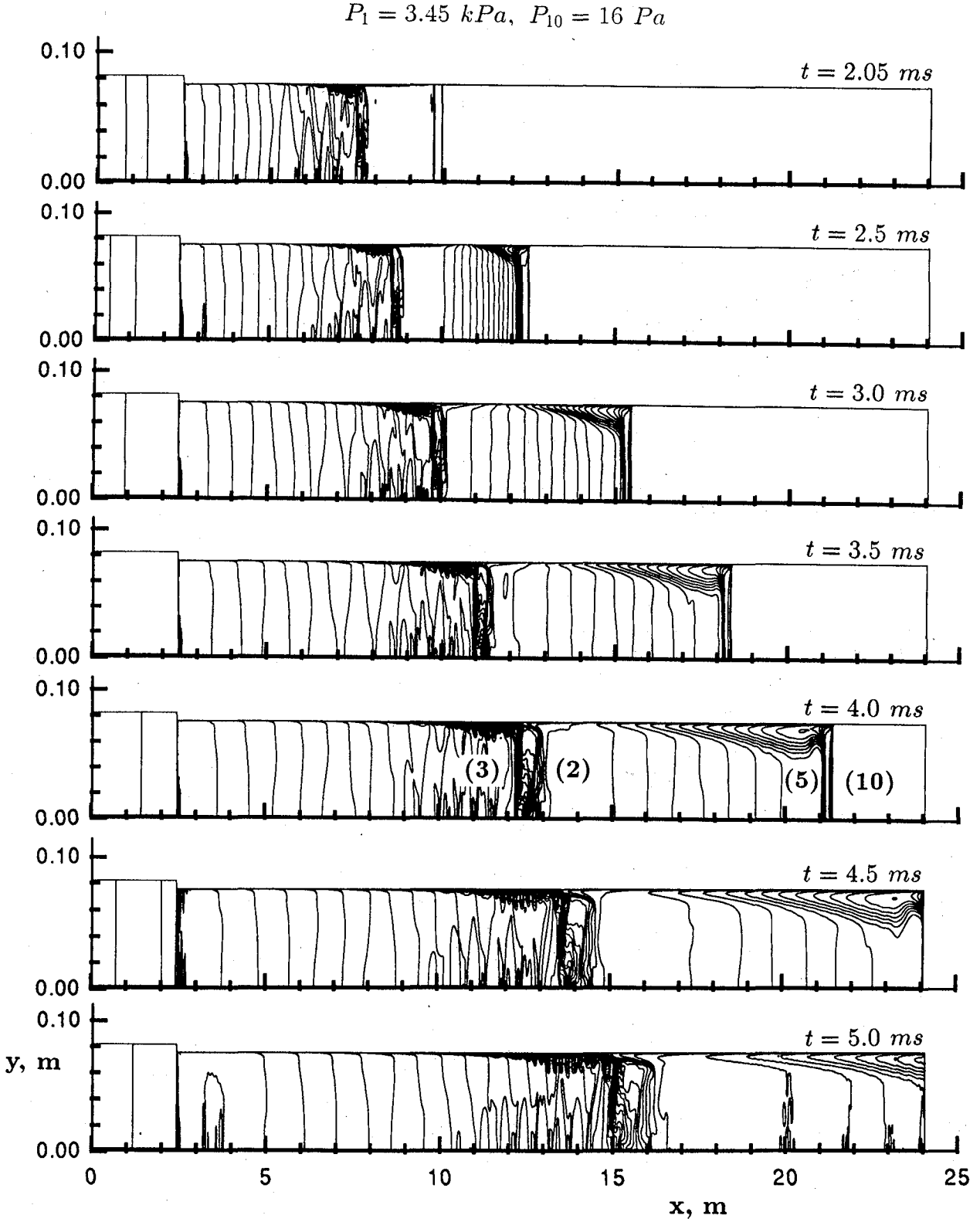

Figure 9: Density contours showing the unsteady expansion of the test gas for case 1.

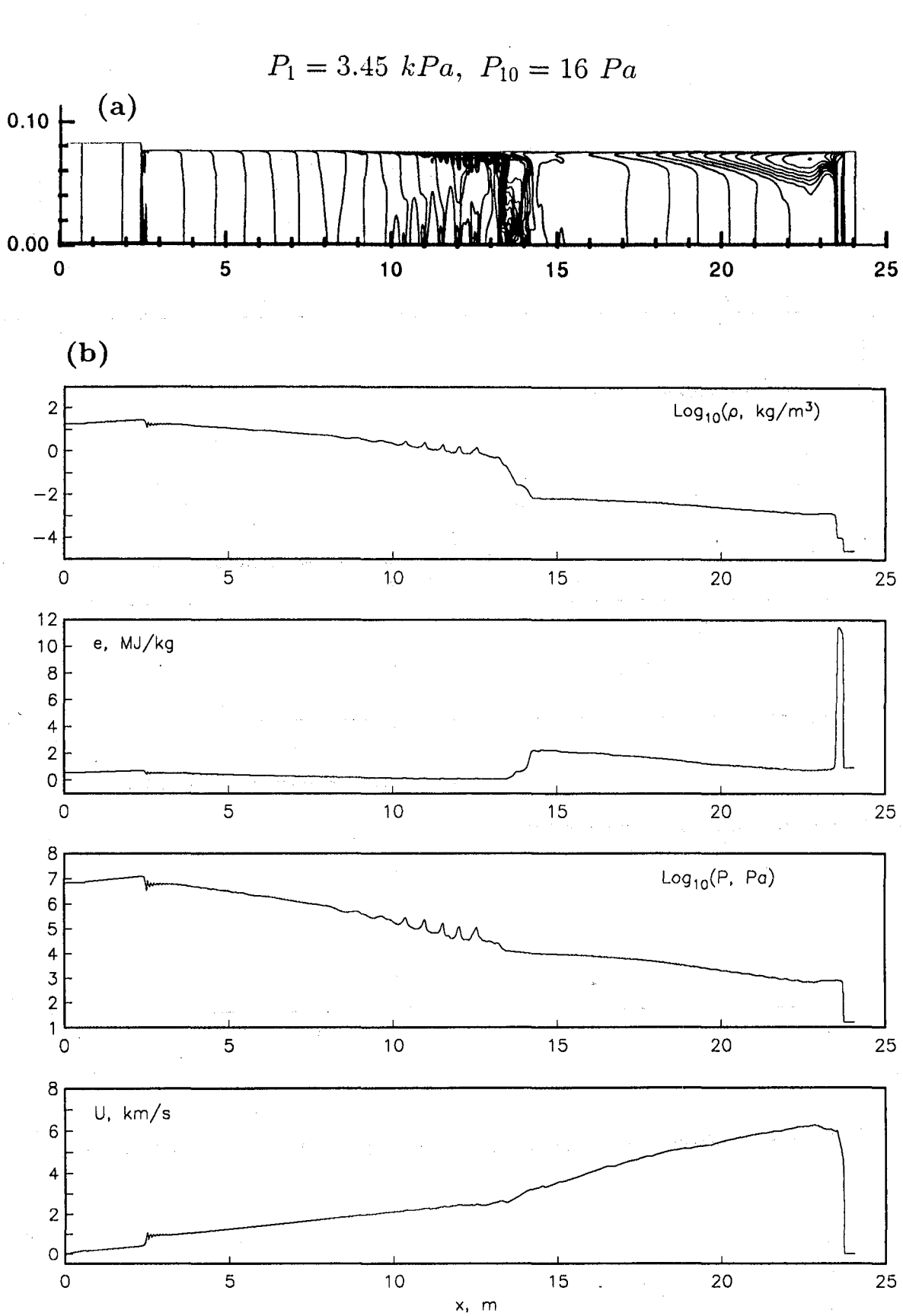

Figure 10: Properties along the axis at $t = 4.4\ ms$ for case 1: (a) density contours; (b) other properties as labelled.

$$P_1 = 3.45\ kPa,\ P_{10} = 16\ Pa$$

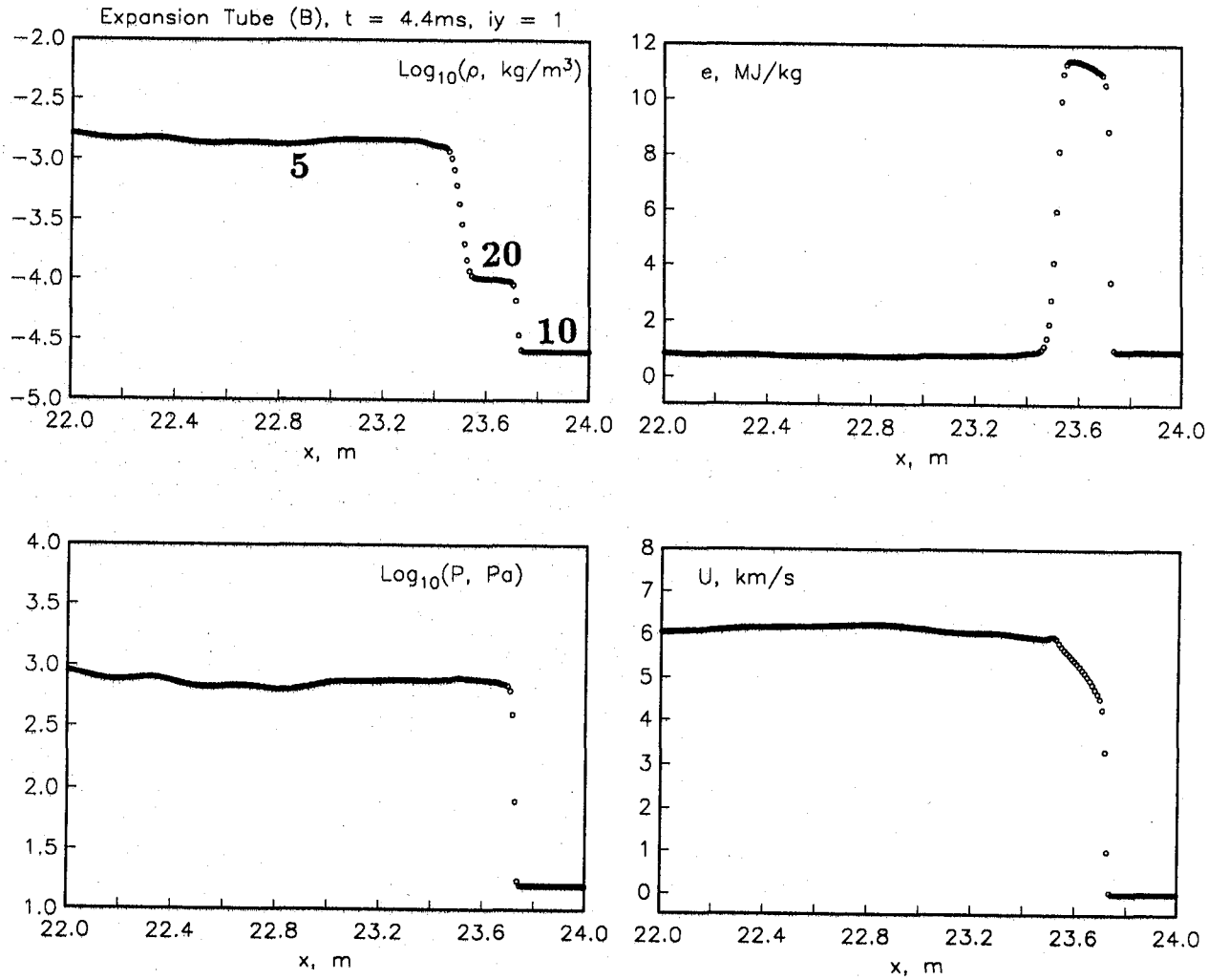

Figure 11: Properties along the axis and near the shock at $t = 4.4\ ms$, case 1.

$$P_1 = 3.45\ kPa,\ P_{10} = 16\ Pa$$

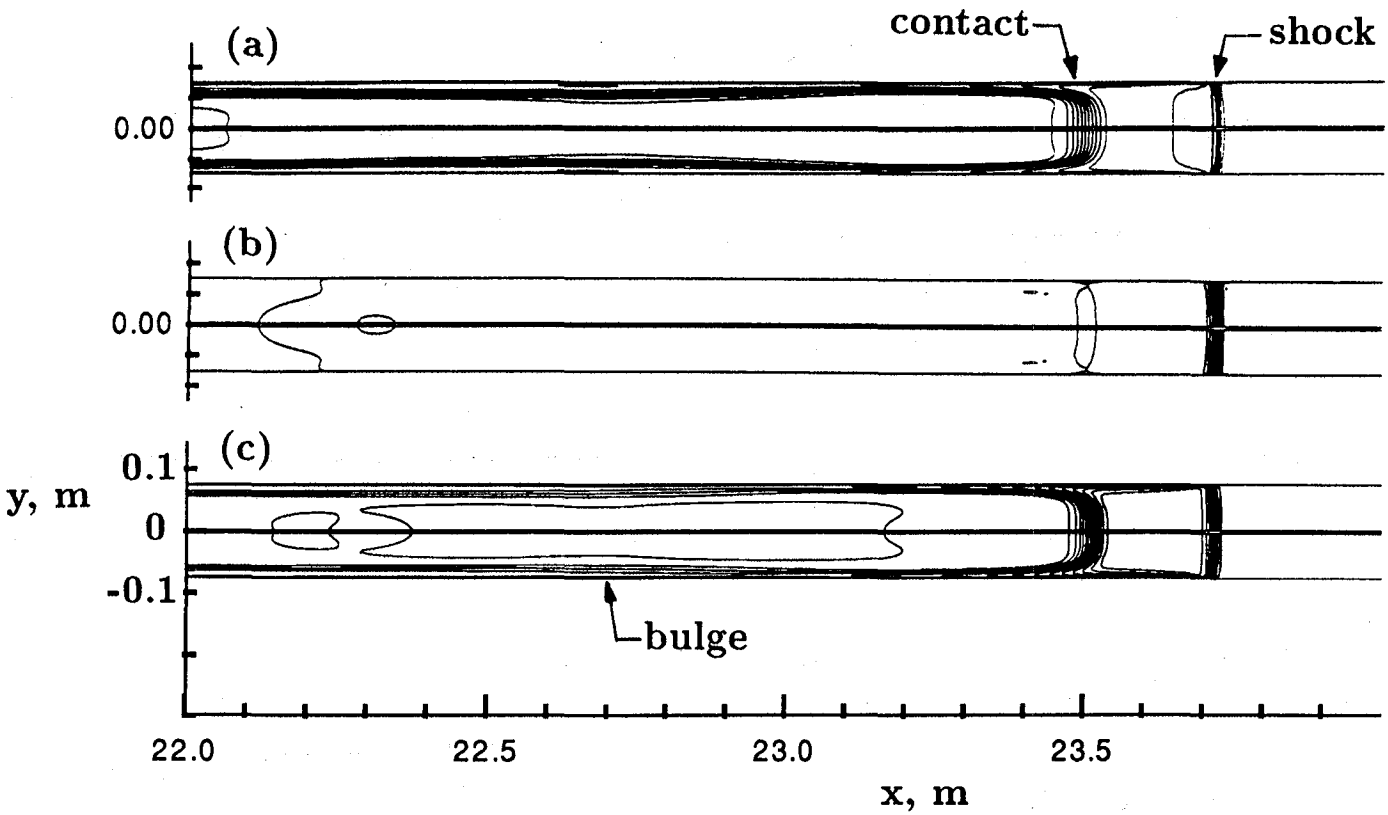

Figure 12: True-shape plots of the flow near the shock at $t = 4.4\ ms$, case 1: (a) density contours; (b) pressure contours; (c) specific-energy contours.

$P_1 = 3.45\ kPa,\ P_{10} = 16\ Pa$

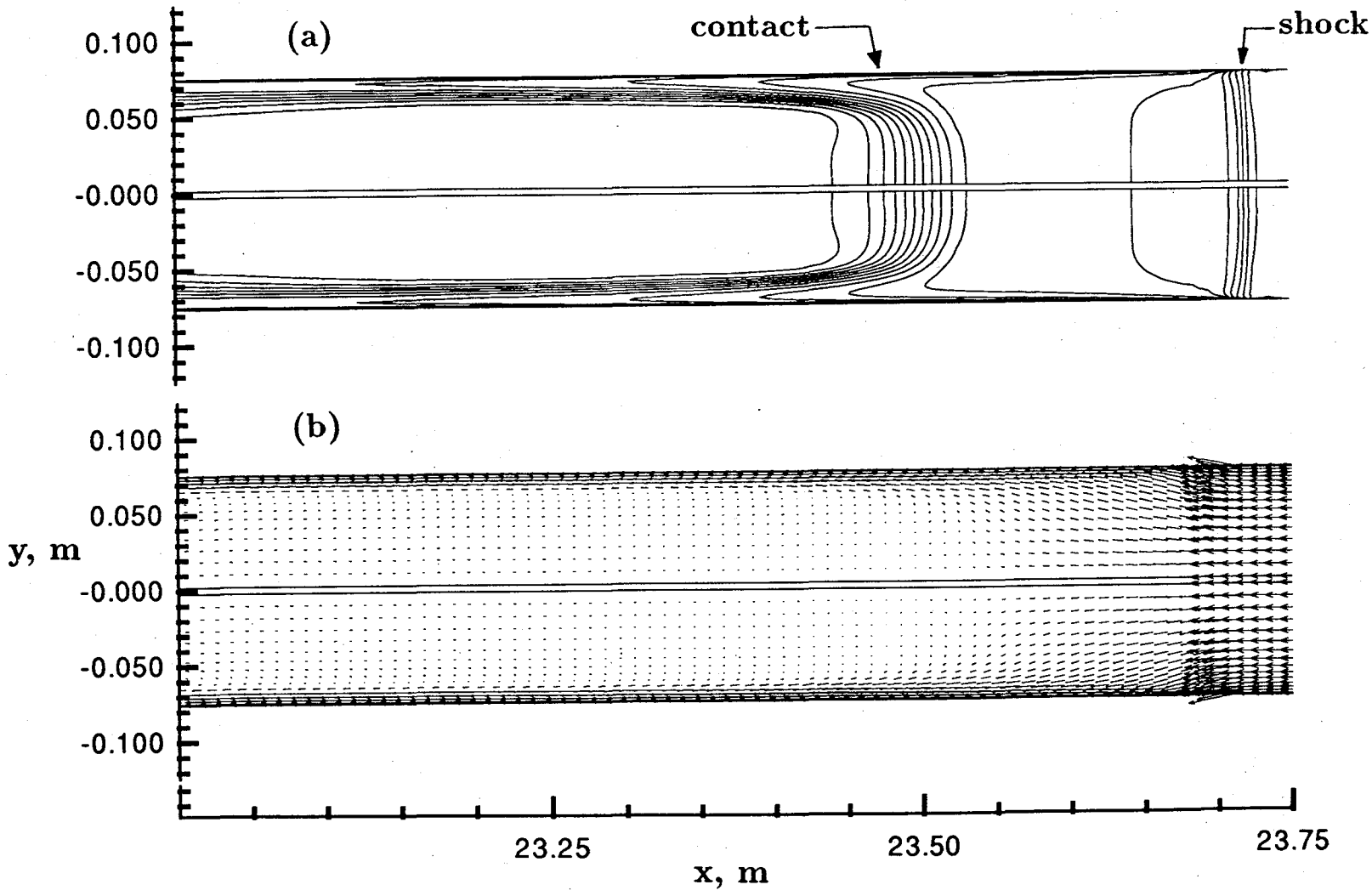

Figure 13: Close-up of the flow near the shock and contact surface at $t = 4.4\ ms$, case 1: (a) density contours; (b) velocity in a frame of reference stationary with respect to the shock and contact.

$$P_1 = 3.45\ kPa,\ P_{10} = 16\ Pa$$

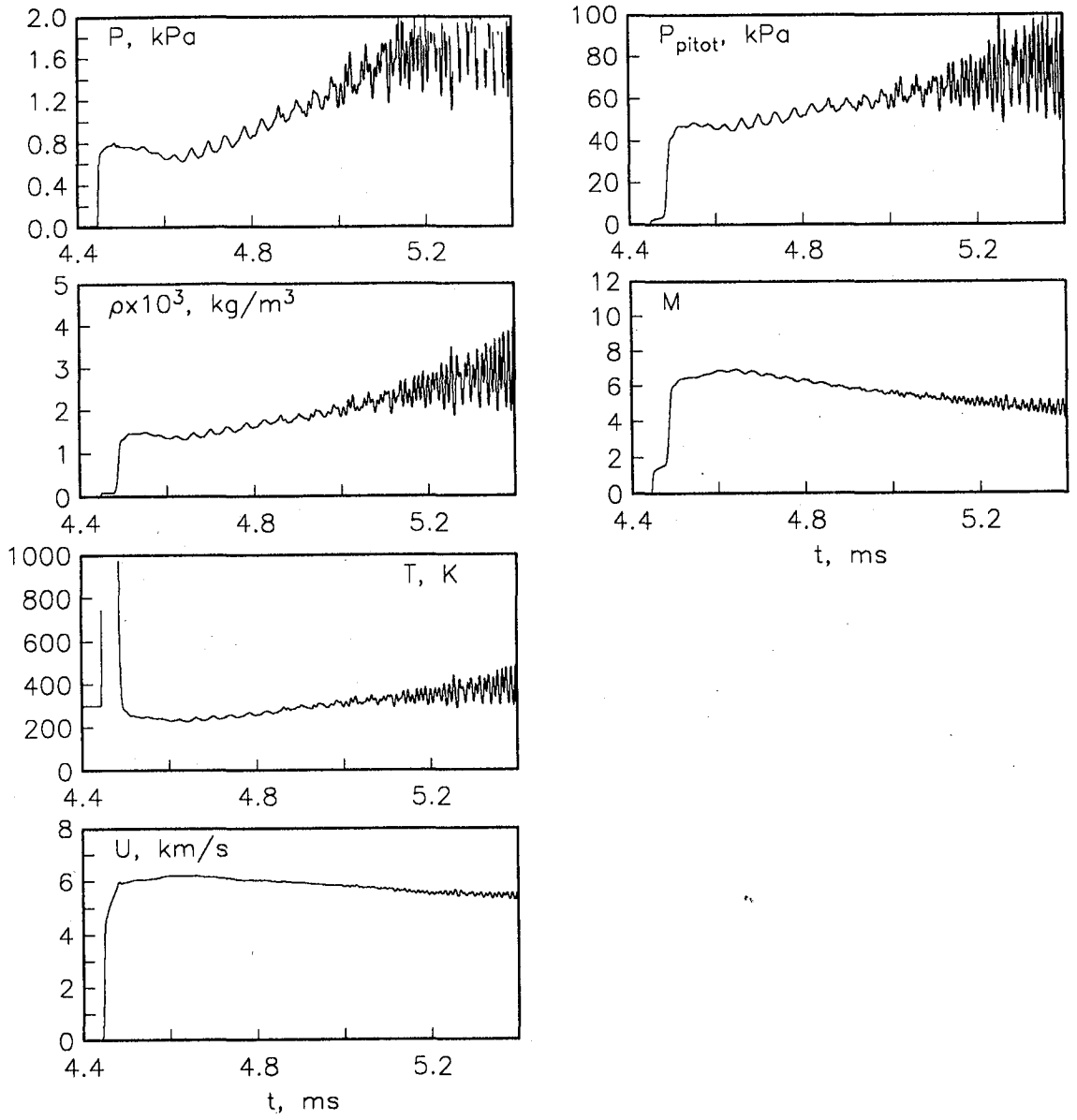

Figure 14: Centreline histories at $x = 24\ m$ for case 1.

$P_1 = 3.45\ kPa,\ P_{10} = 16\ Pa$

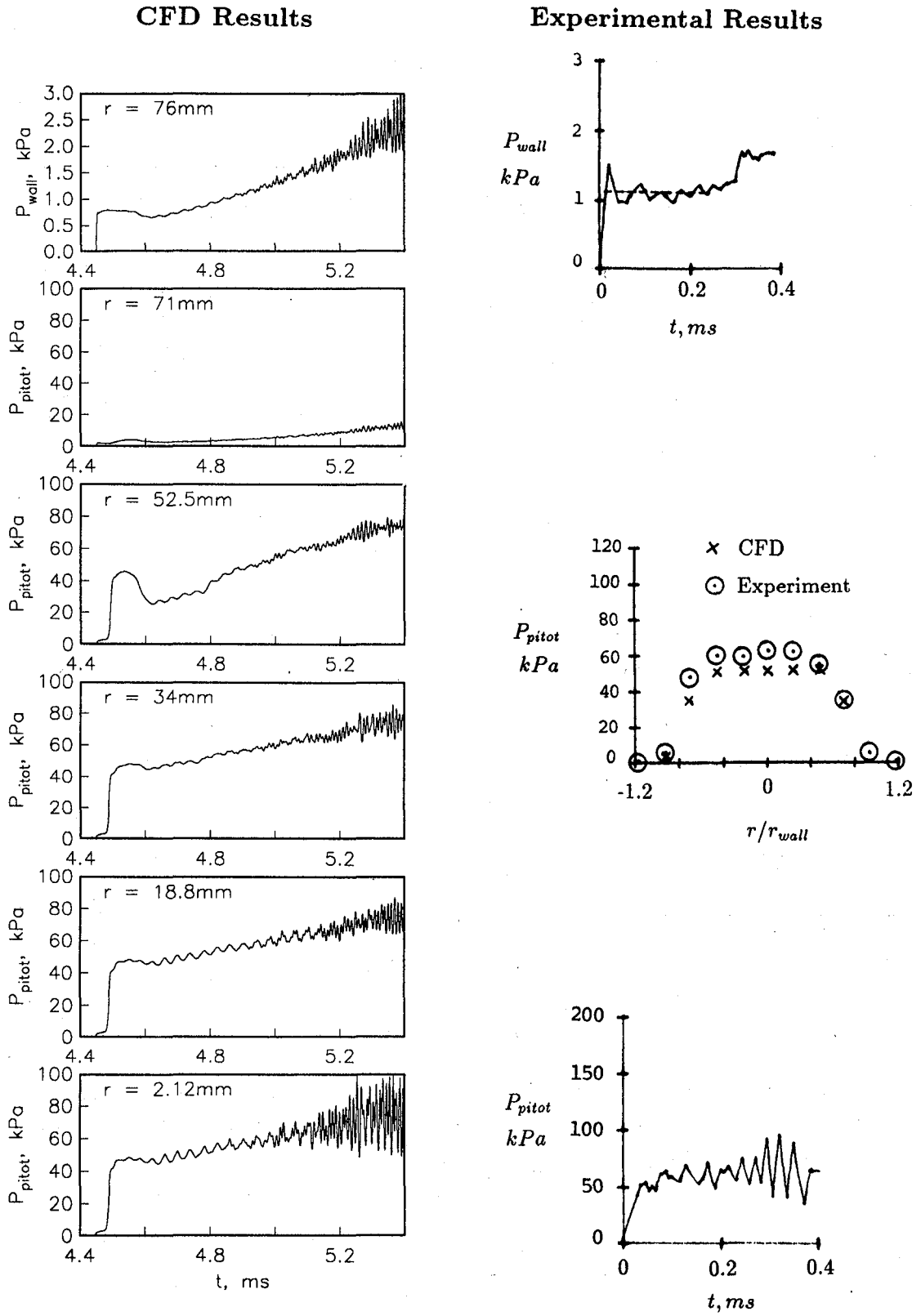

Figure 15: Comparison of wall pressure and pitot pressure with experiment (case 1, $x = 24\ m$). The experimental data is taken from Shinn and Miller (1978).

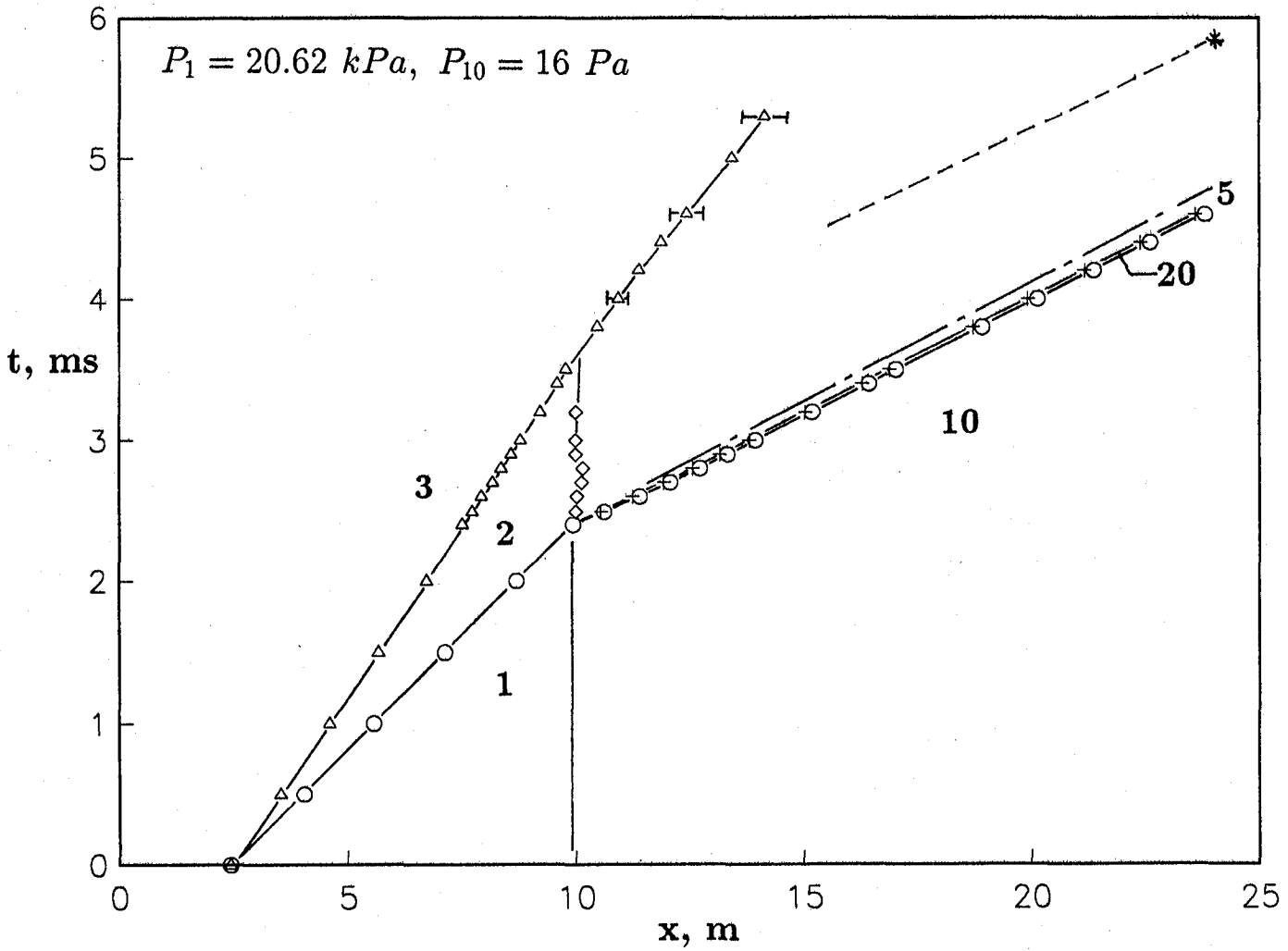

Figure 16: Wave diagram for case 2. ○ = shock; △ = driver-gas/test-gas interface; + = test-gas/acceleration-gas interface; long dash = downstream tail of the unsteady expansion; ◇ = upstream head of the unsteady expansion; short dash = reflected expansion.

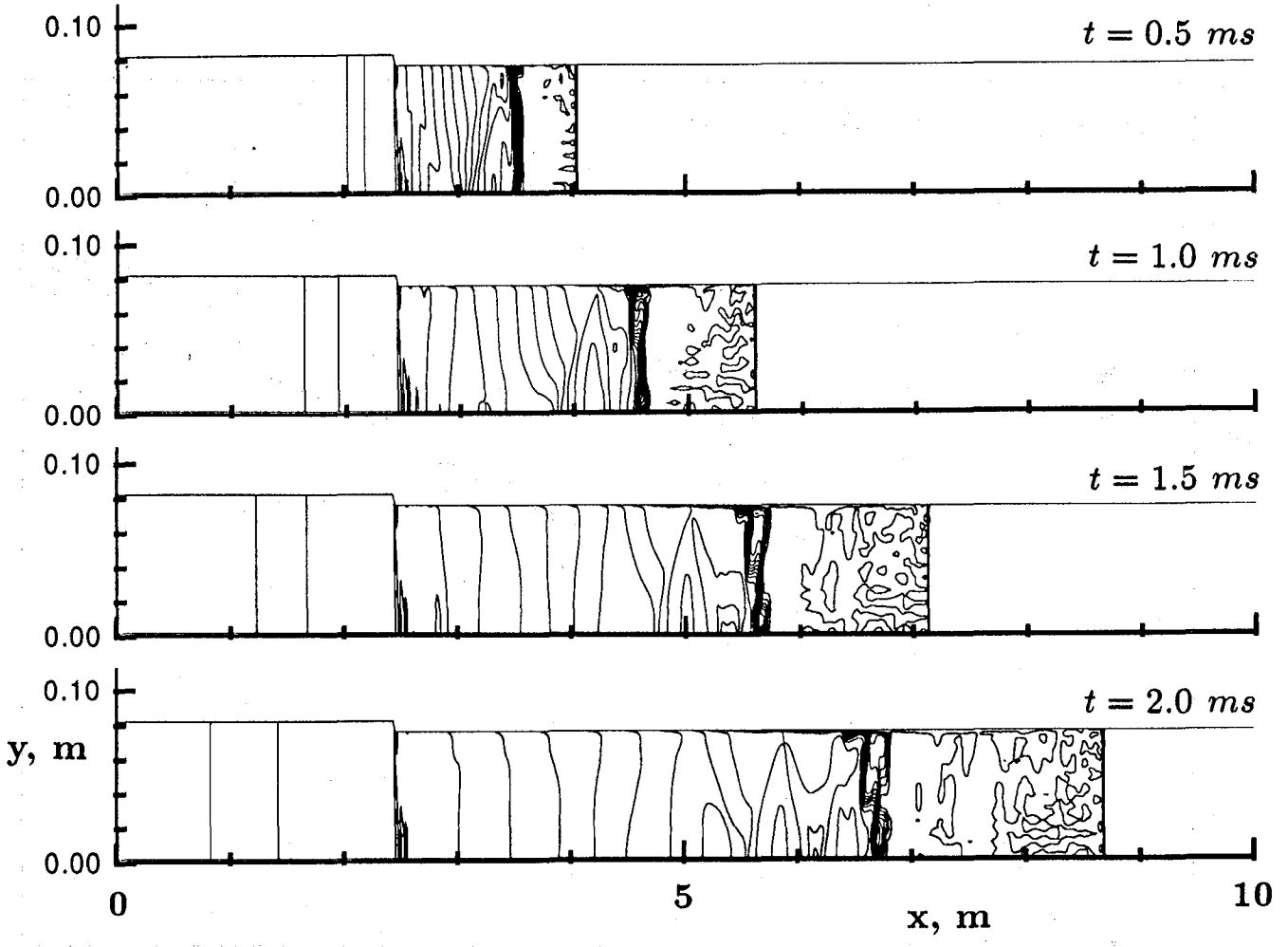

Figure 17: Density contours showing the shock compression of the test gas for case 2.

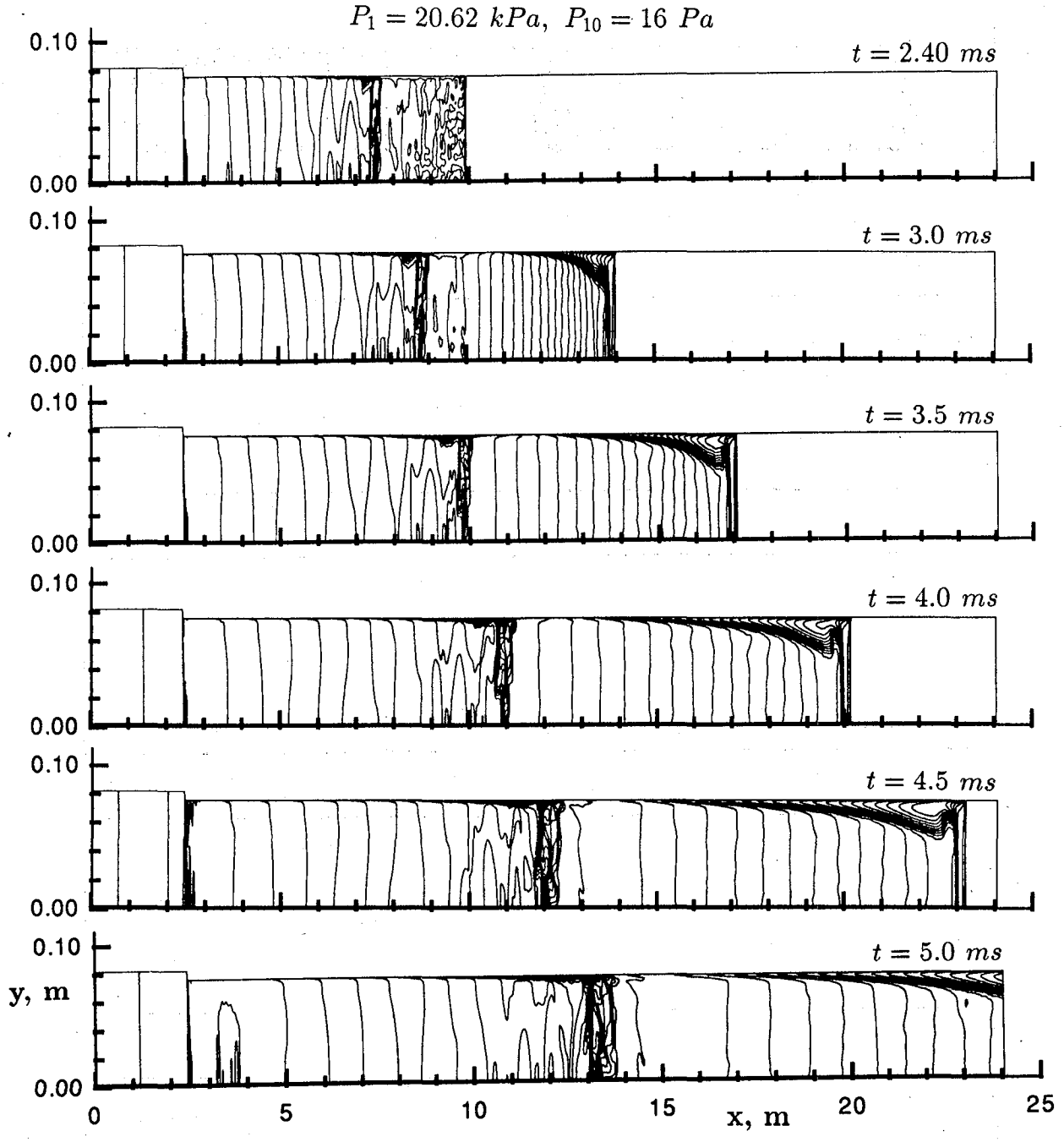

Figure 18: Density contours showing the unsteady expansion of the test gas for case 2.

$P_1 = 20.62\ kPa,\ P_{10} = 16\ Pa$

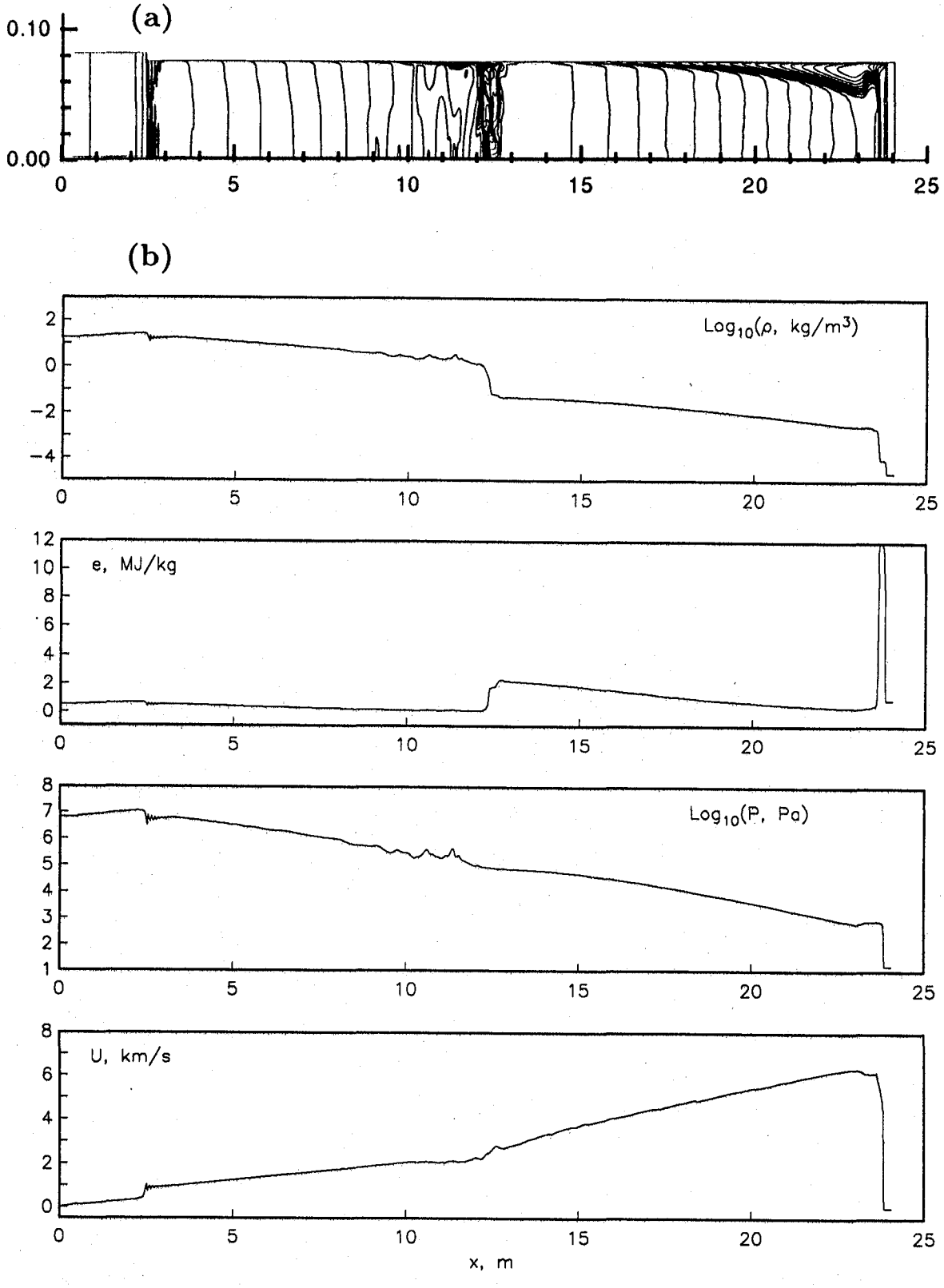

Figure 19: Properties along the axis at $t = 4.6\ ms$ for case 2: (a) density contours; (b) other properties as labelled.

$$P_1 = 20.62\ kPa,\ P_{10} = 16\ Pa$$

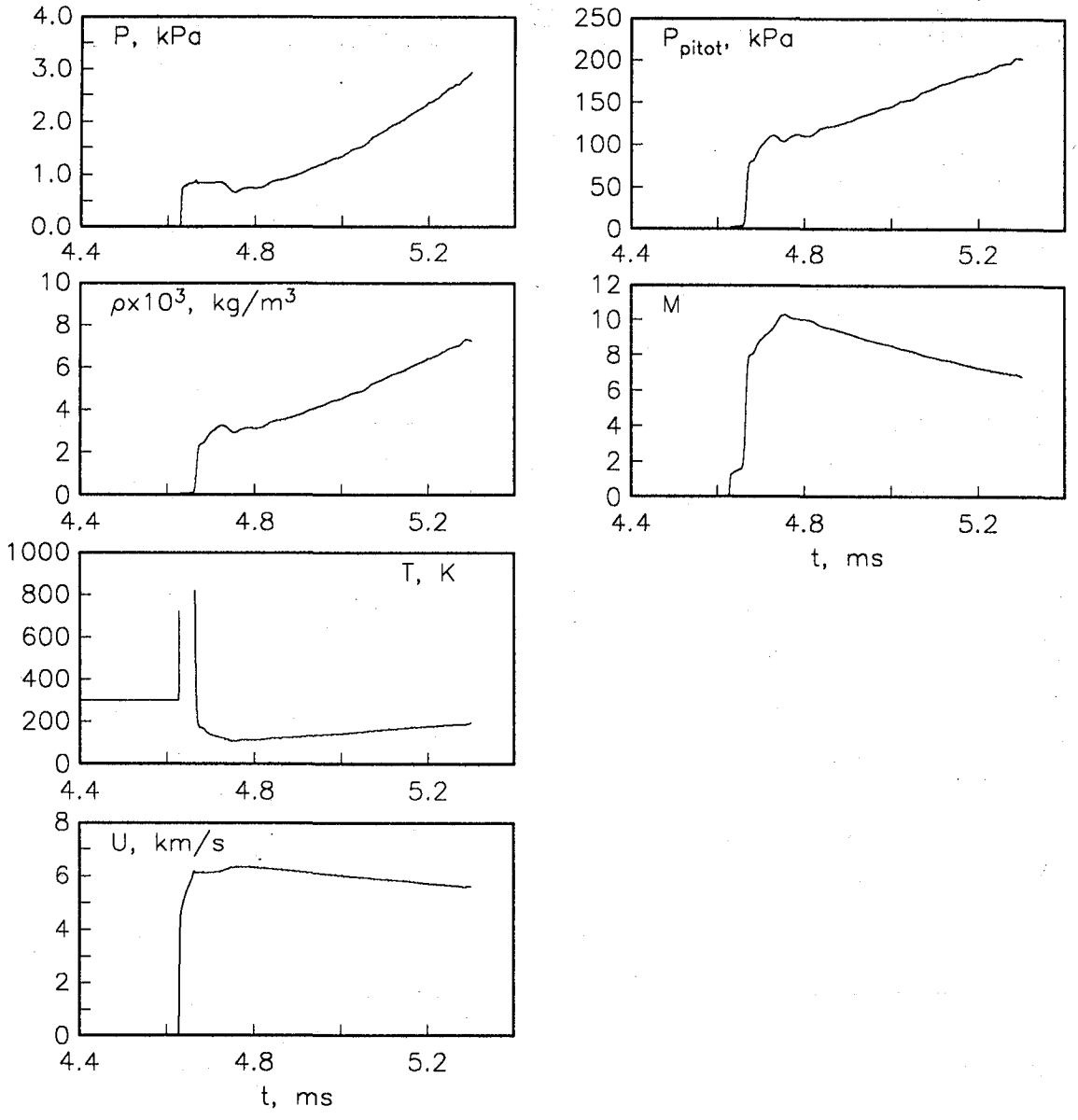

Figure 20: Centreline histories at $x = 24\ m$ for case 2.

$$P_1 = 20.62\ kPa,\ P_{10} = 16\ Pa$$

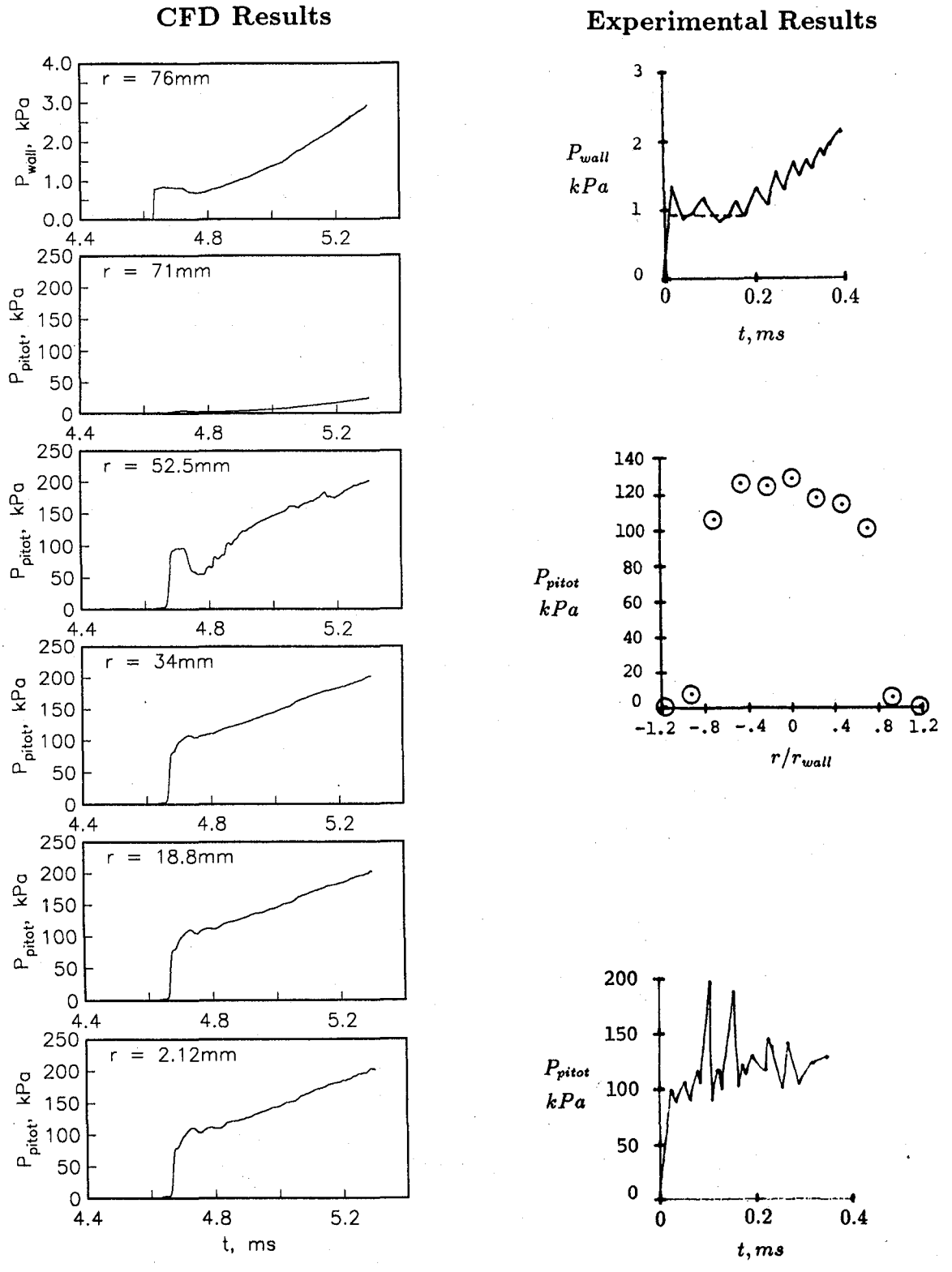

Figure 21: Comparison of wall pressure and pitot pressure with experiment (case 2, $x = 24\ m$). The experimental data is taken from Shinn and Miller (1978).

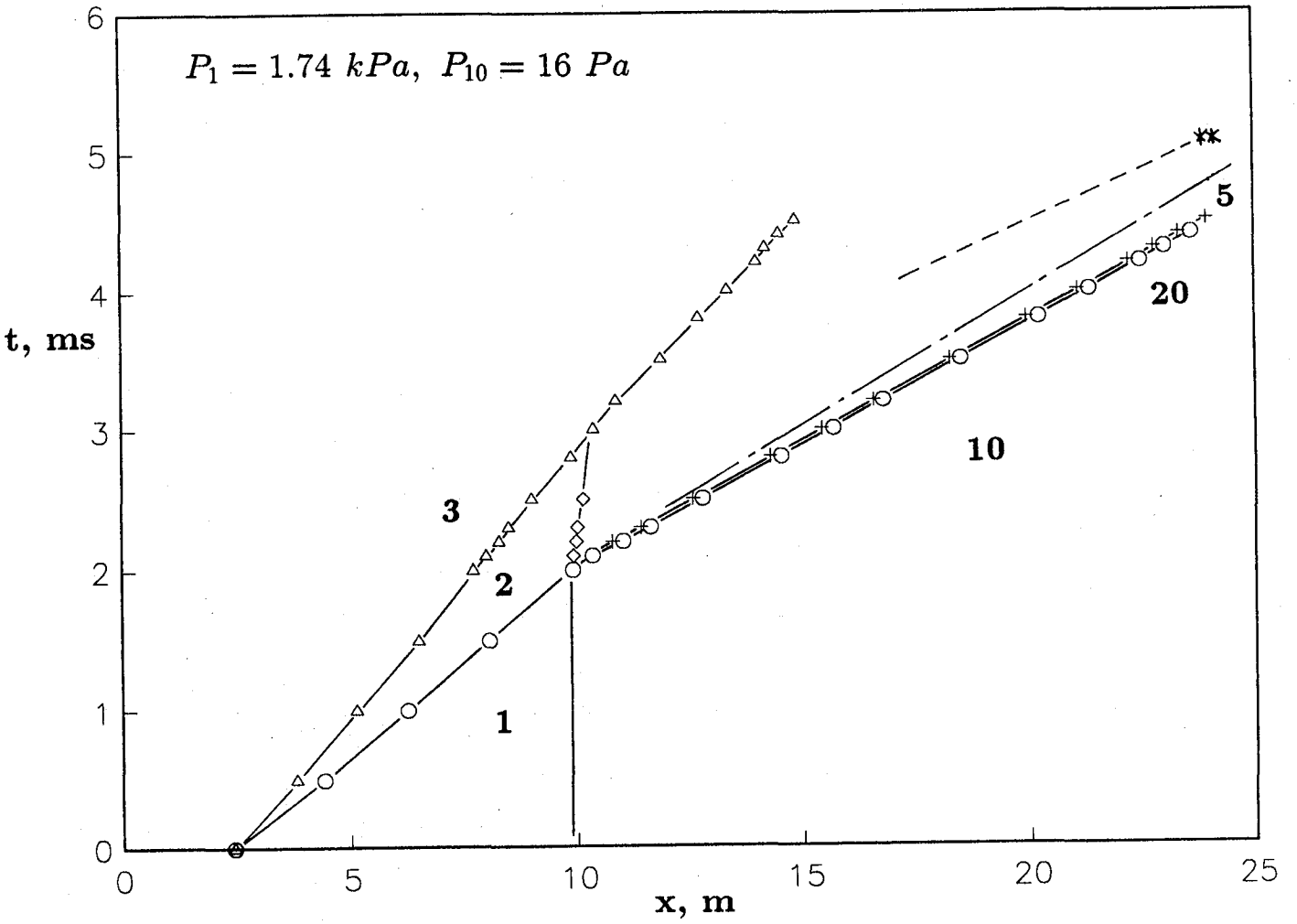

Figure 22: Wave diagram for case 3. ◯ = shock; △ = driver-gas/test-gas interface; + = test-gas/acceleration-gas interface; long dash = downstream tail of the unsteady expansion; ◇ = upstream head of the unsteady expansion; short dash = reflected expansion.

$$P_1 = 1.74\ kPa,\ P_{10} = 16\ Pa$$

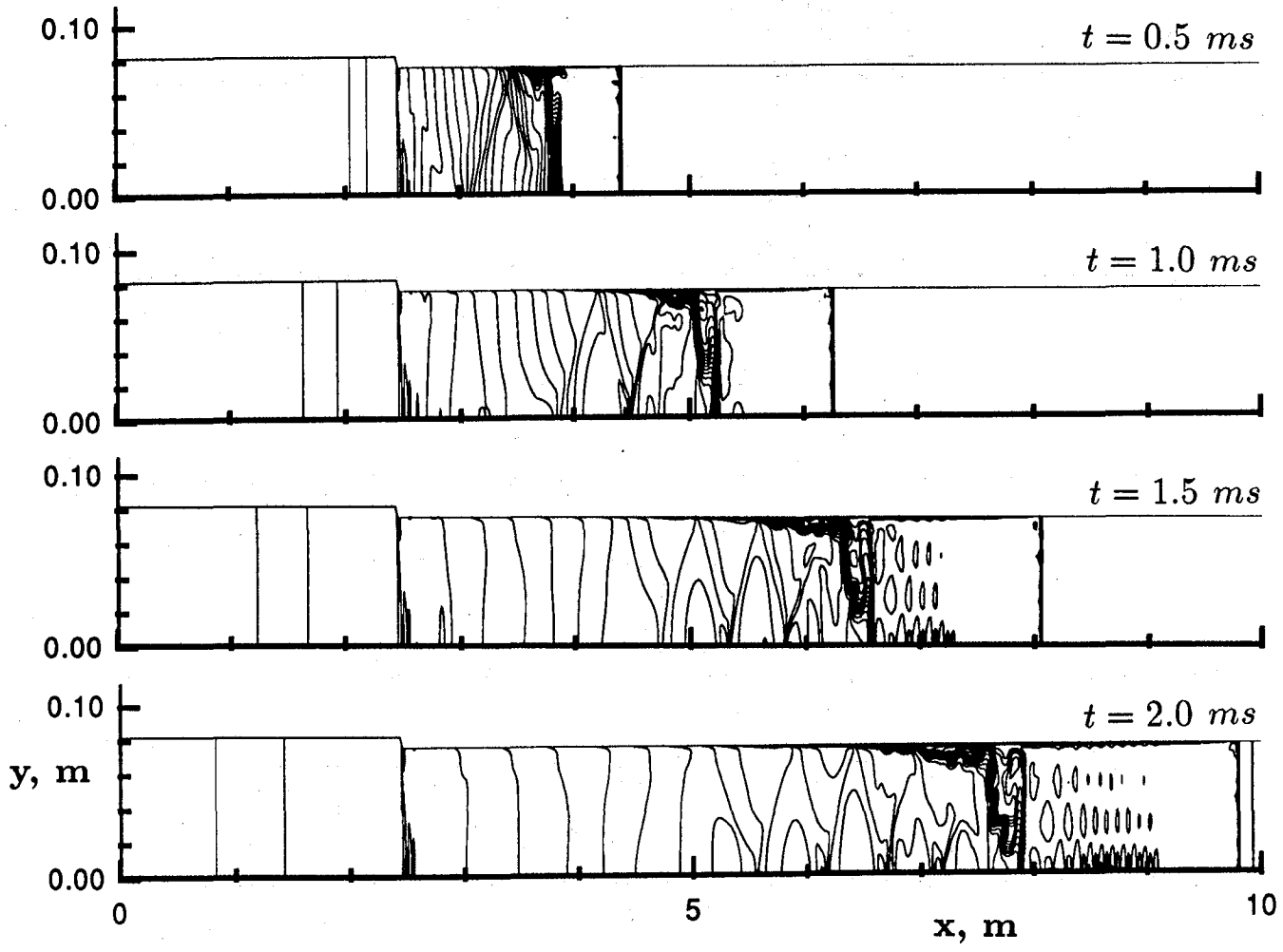

Figure 23: Density contours showing the shock compression of the test gas for case 3.

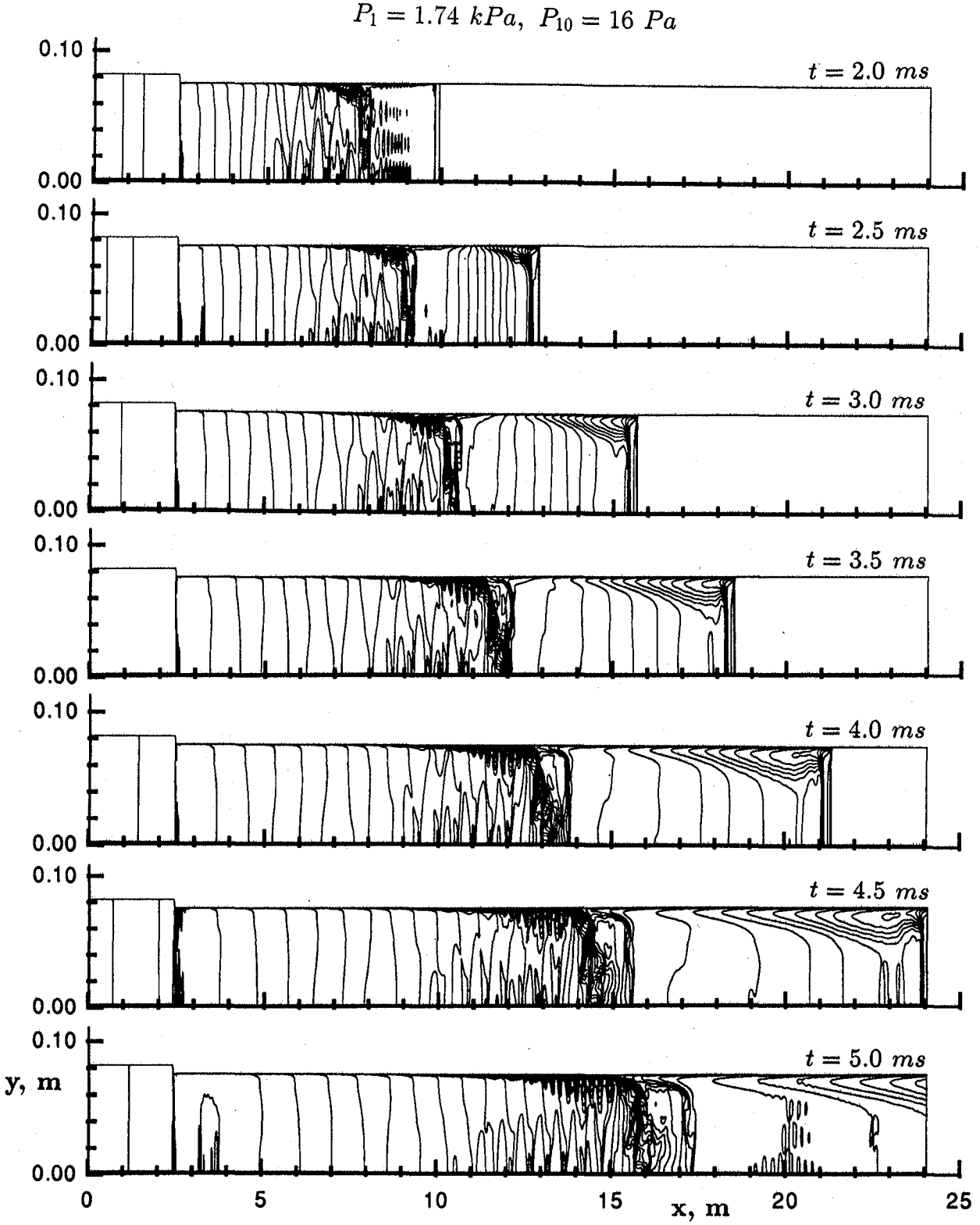

Figure 24: Density contours showing the unsteady expansion of the test gas for case 3.

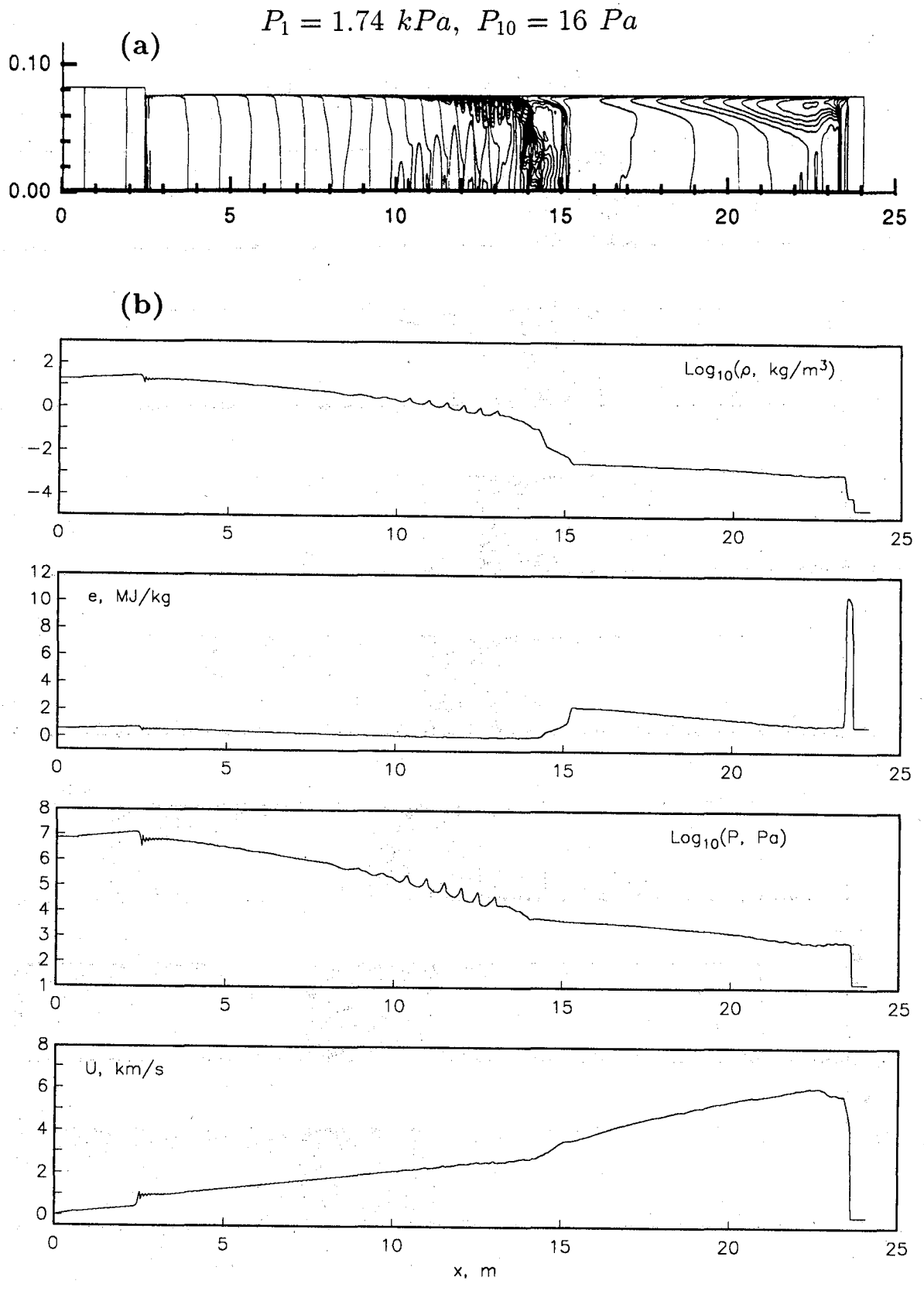

Figure 25: Properties along the axis at $t = 4.4\ ms$ for case 3: (a) density contours; (b) other properties as labelled.

$$P_1 = 1.74\ kPa,\ P_{10} = 16\ Pa$$

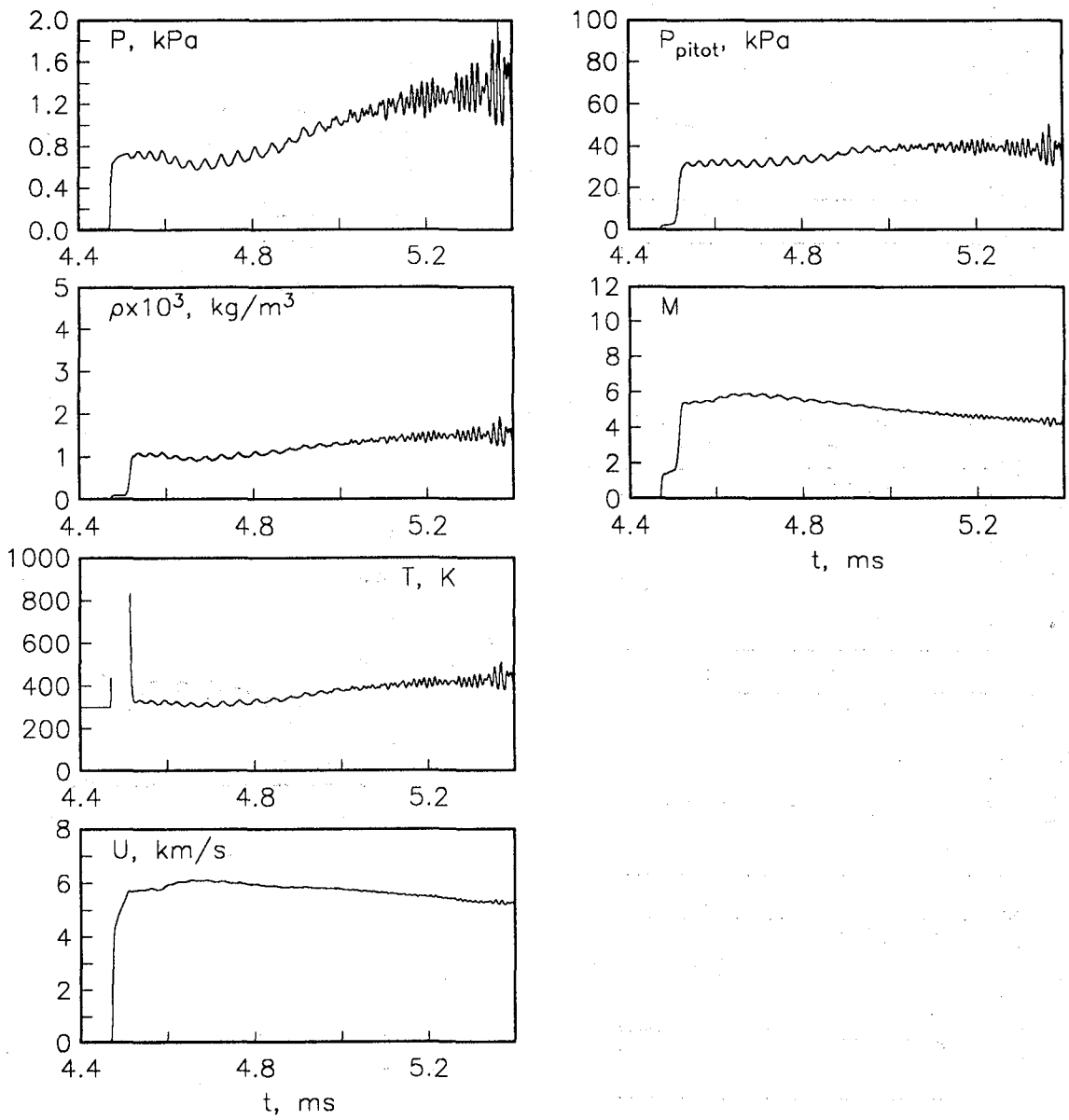

Figure 26: Centreline histories at $x = 24\ m$ for case 3.

$P_1 = 1.74\ kPa,\ P_{10} = 16\ Pa$

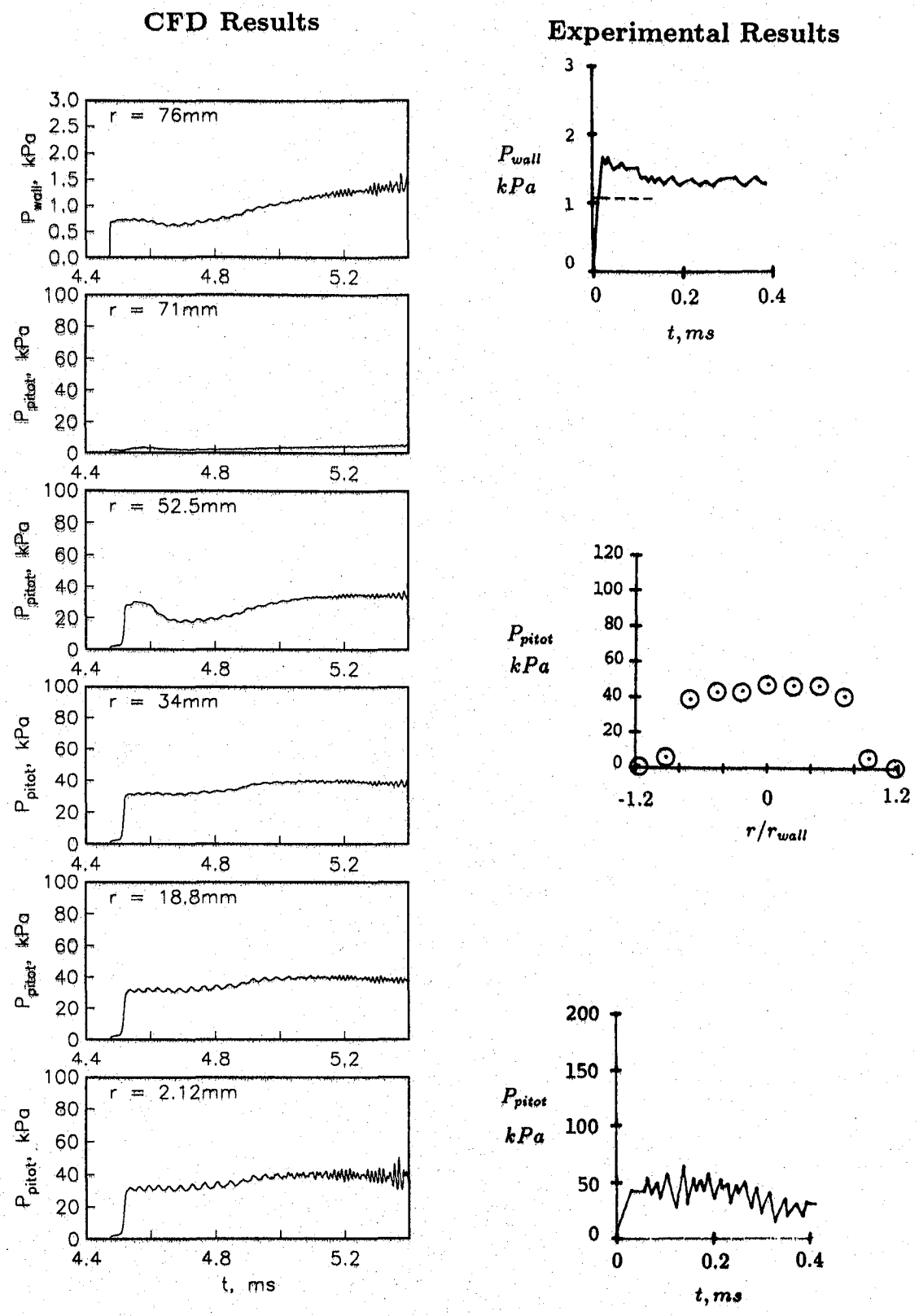

Figure 27: Comparison of wall pressure and pitot pressure with experiment (case 3, $x = 24\ m$). The experimental data is taken from Shinn and Miller (1978).

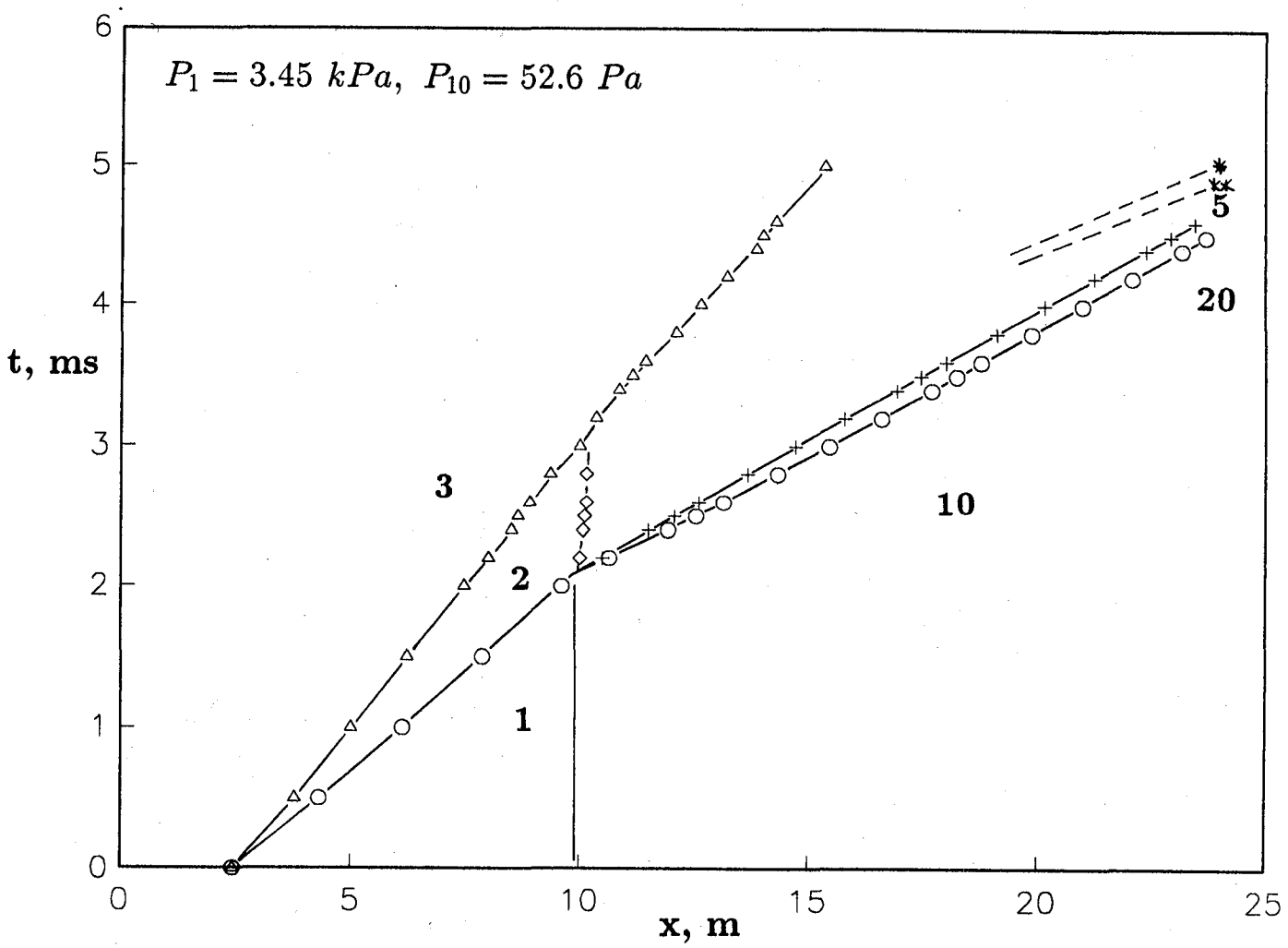

Figure 28: Wave diagram for case 4. ○ = shock; △ = driver-gas/test-gas interface; + = test-gas/acceleration-gas interface; long dash = downstream tail of the unsteady expansion; ◇ = upstream head of the unsteady expansion; short dash = reflected expansion.

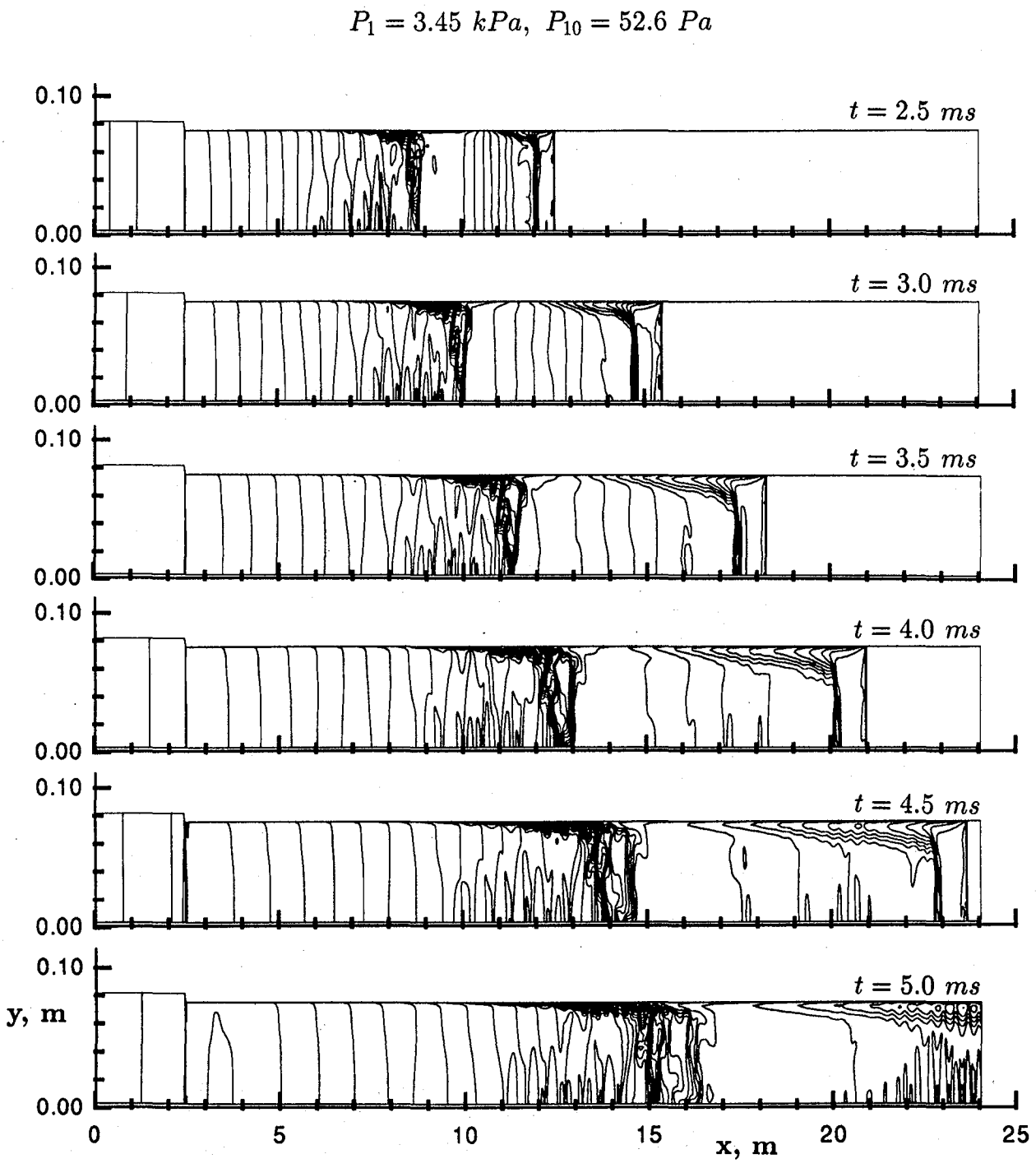

Figure 29: Density contours showing the unsteady expansion of the test gas for case 4.

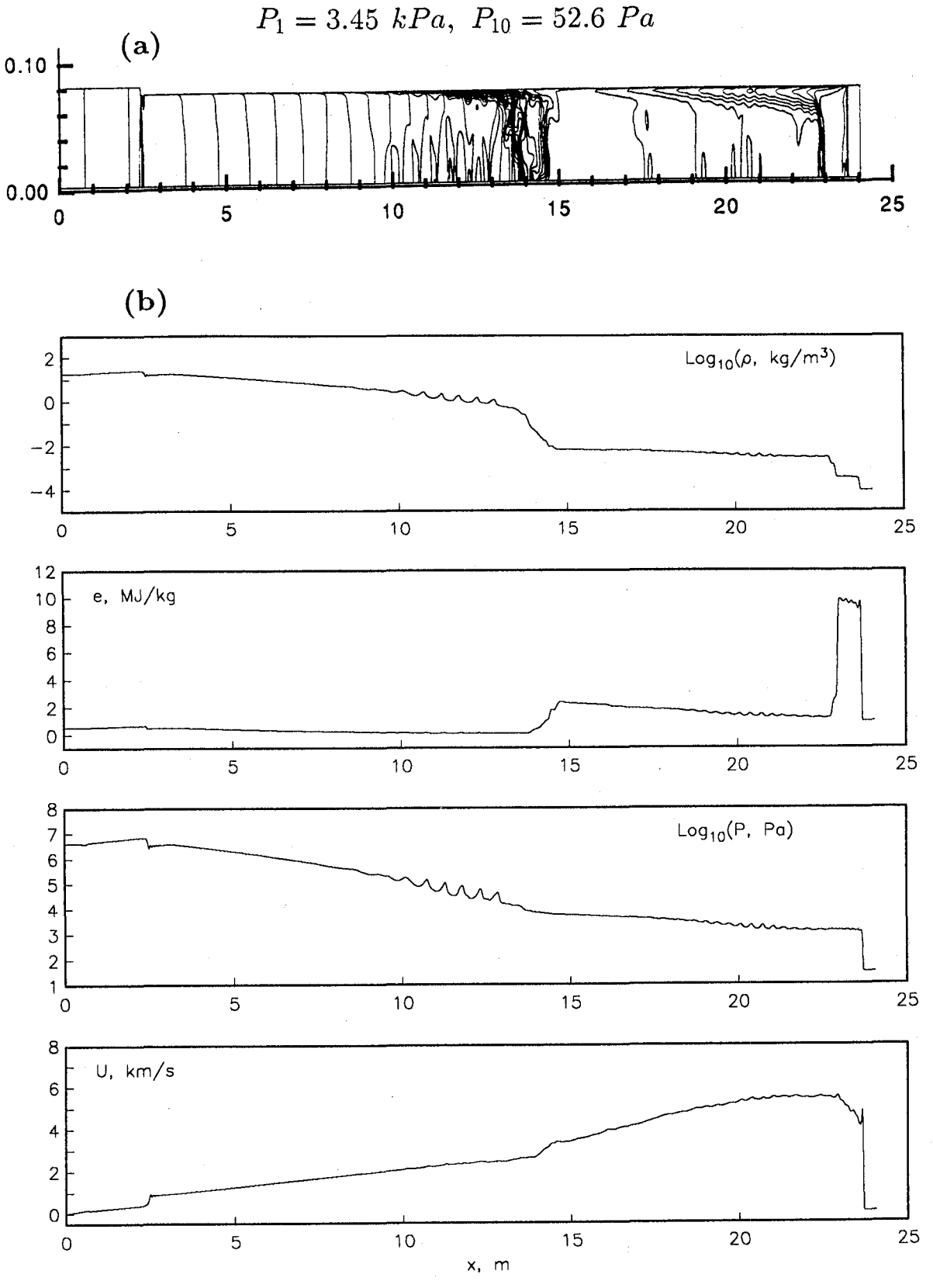

Figure 30: Properties along the axis at $t = 4.5\ ms$ for case 4: (a) density contours; (b) other properties as labelled.

$$P_1 = 3.45\ kPa,\ P_{10} = 52.6\ Pa$$

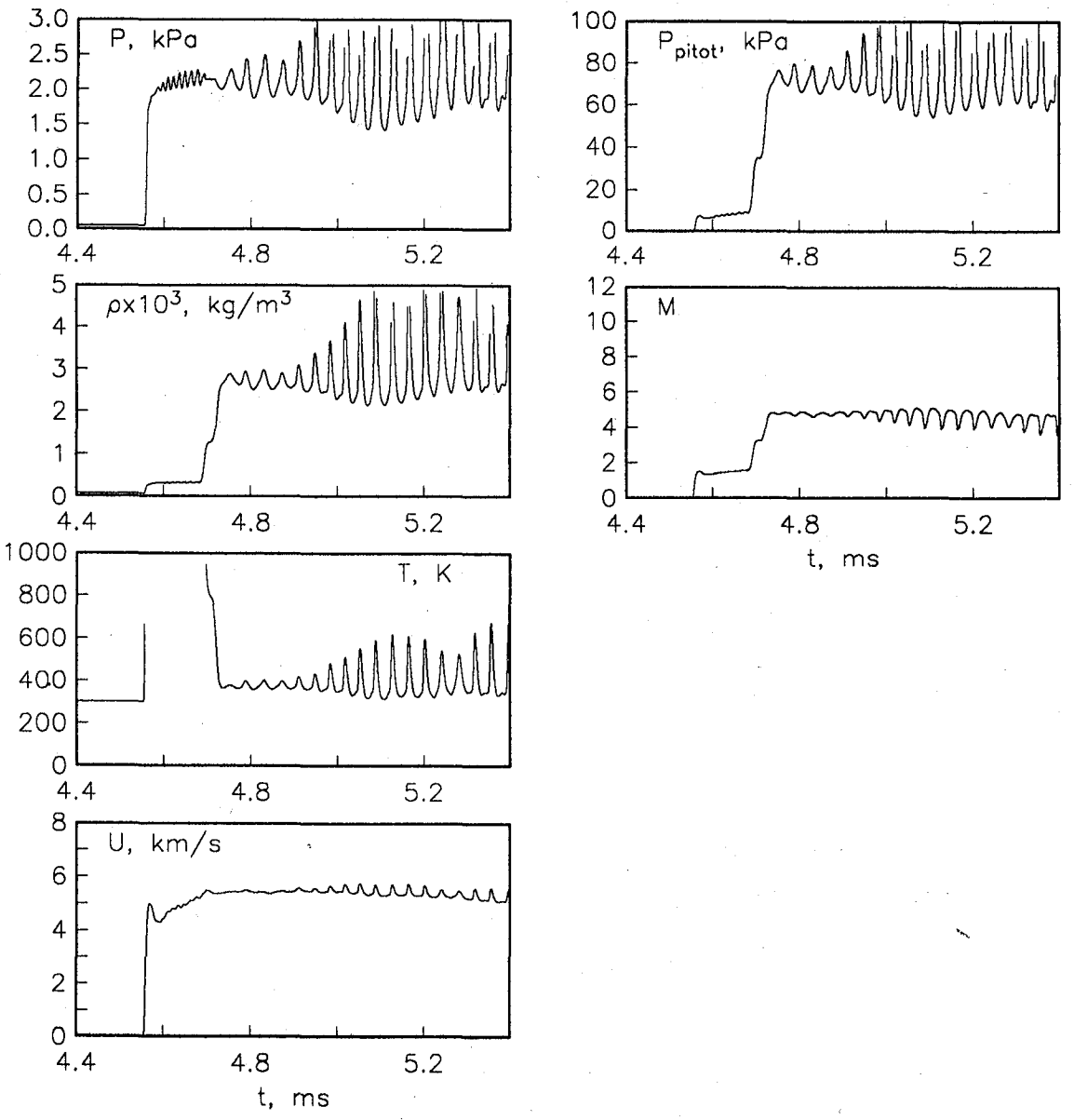

Figure 31: Centreline histories at $x = 24\ m$ for case 4.

$P_1 = 3.45\ kPa,\ P_{10} = 52.6\ Pa$

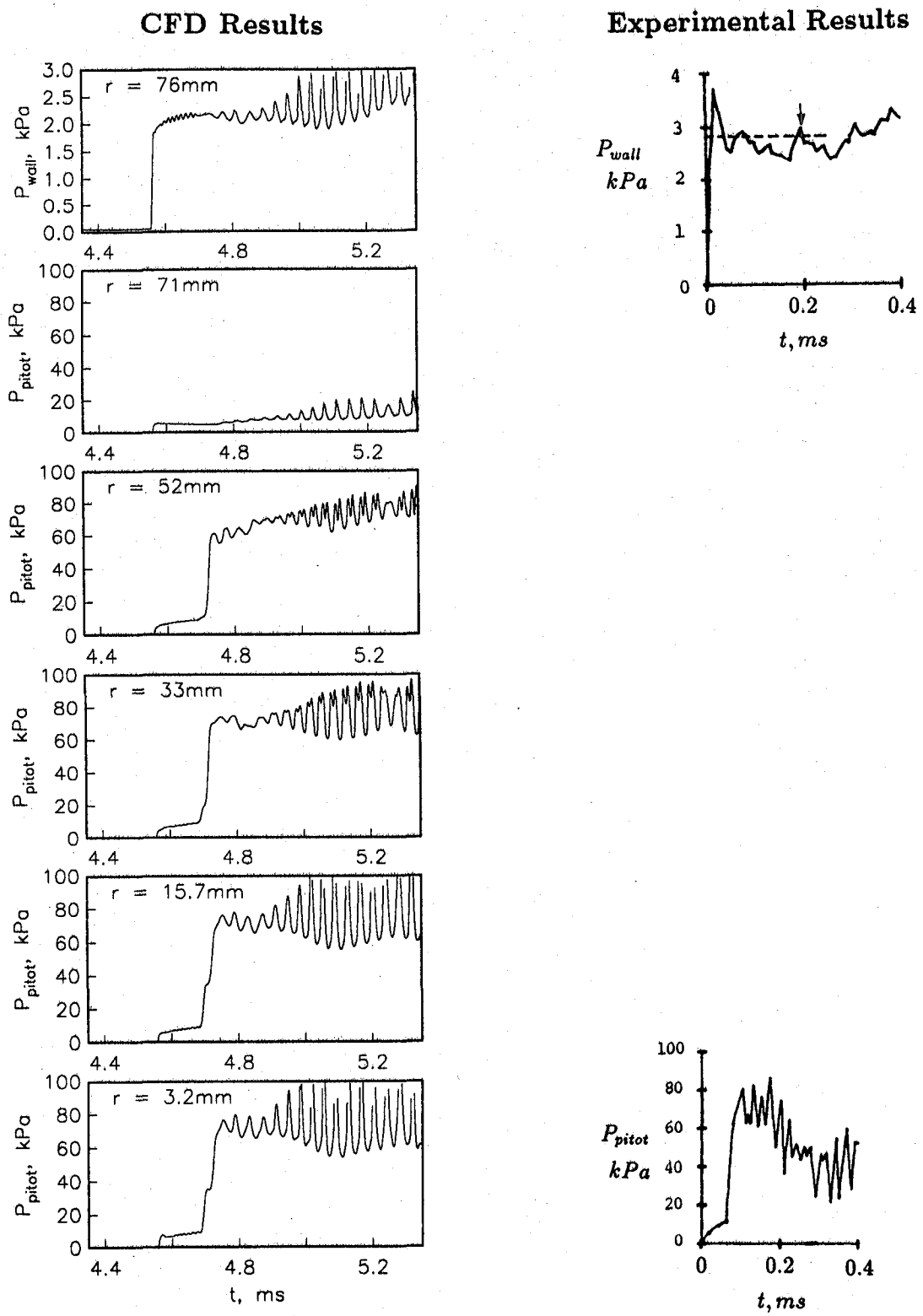

Figure 32: Comparison of wall pressure and pitot pressure with experiment (case 4, $x = 24\ m$). The experimental data is taken from Shinn and Miller (1978).

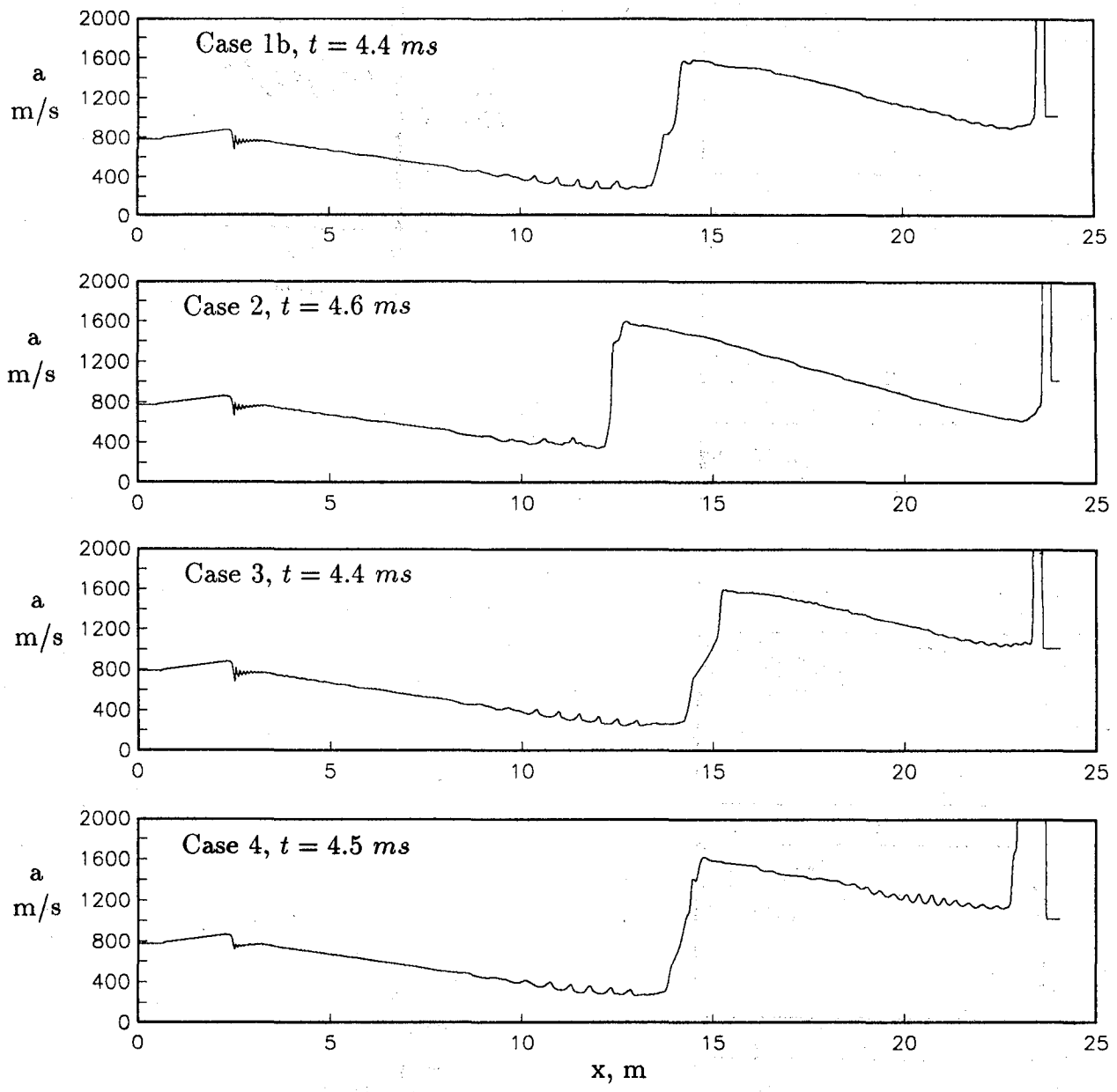

Figure 33: Axial variation of the sound speed for each case shortly before arrival of the shock at the acceleration-tube exit.

$P_1 = 3.45\ kPa,\ P_{10} = 16\ Pa$

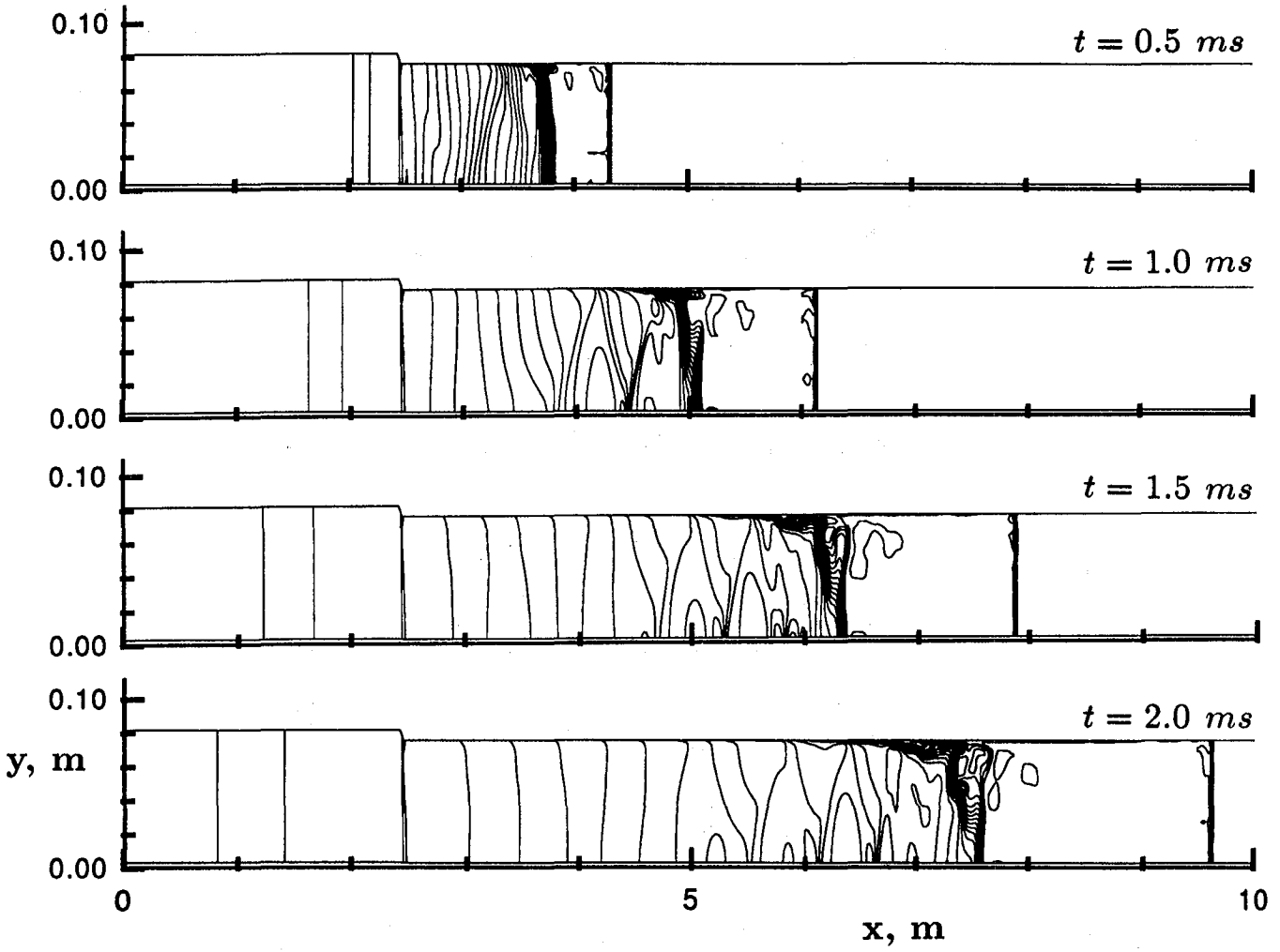

Figure 34: Density contours showing the shock compression of the test gas for case 1a.

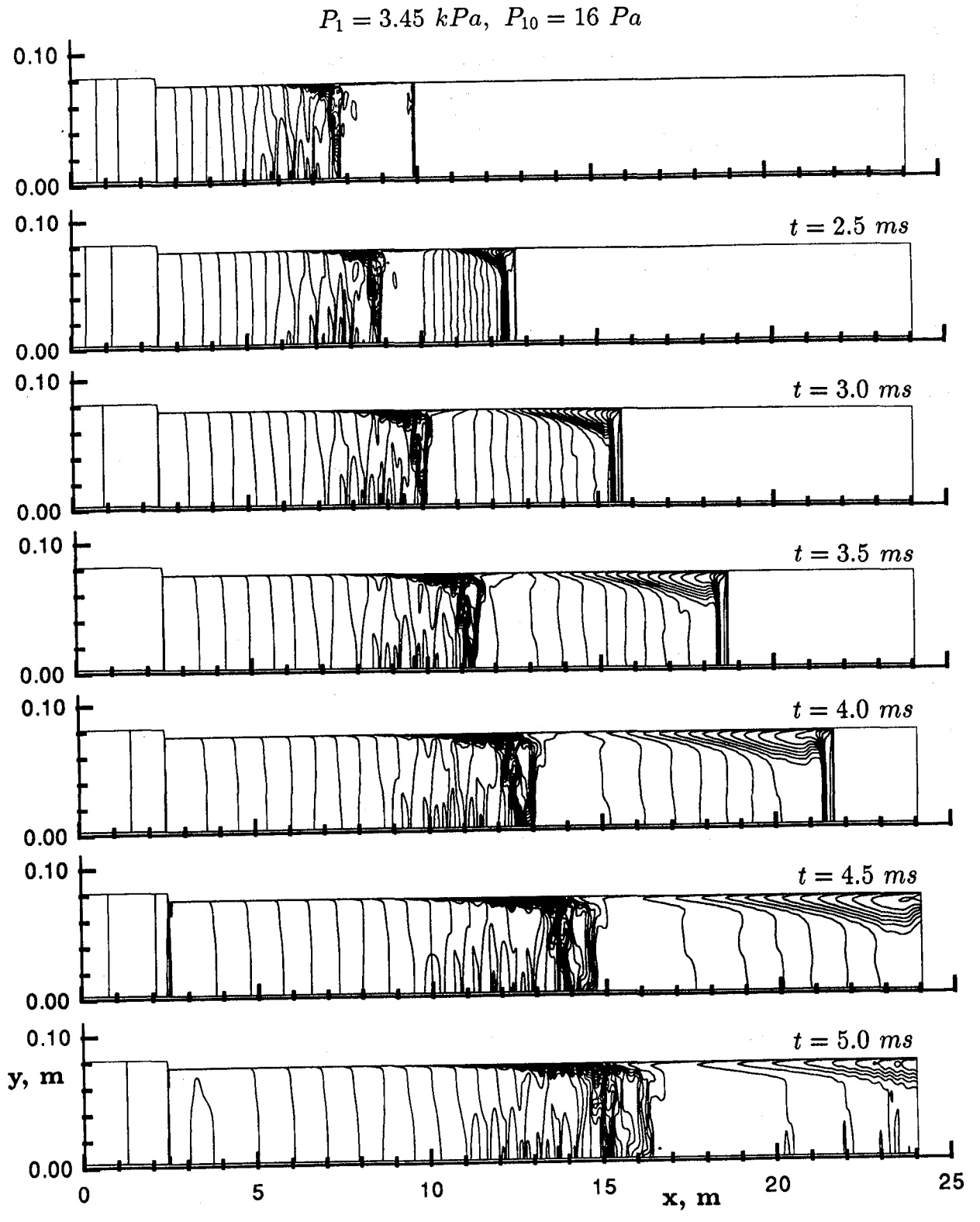

Figure 35: Density contours showing the unsteady expansion of the test gas for case 1a.

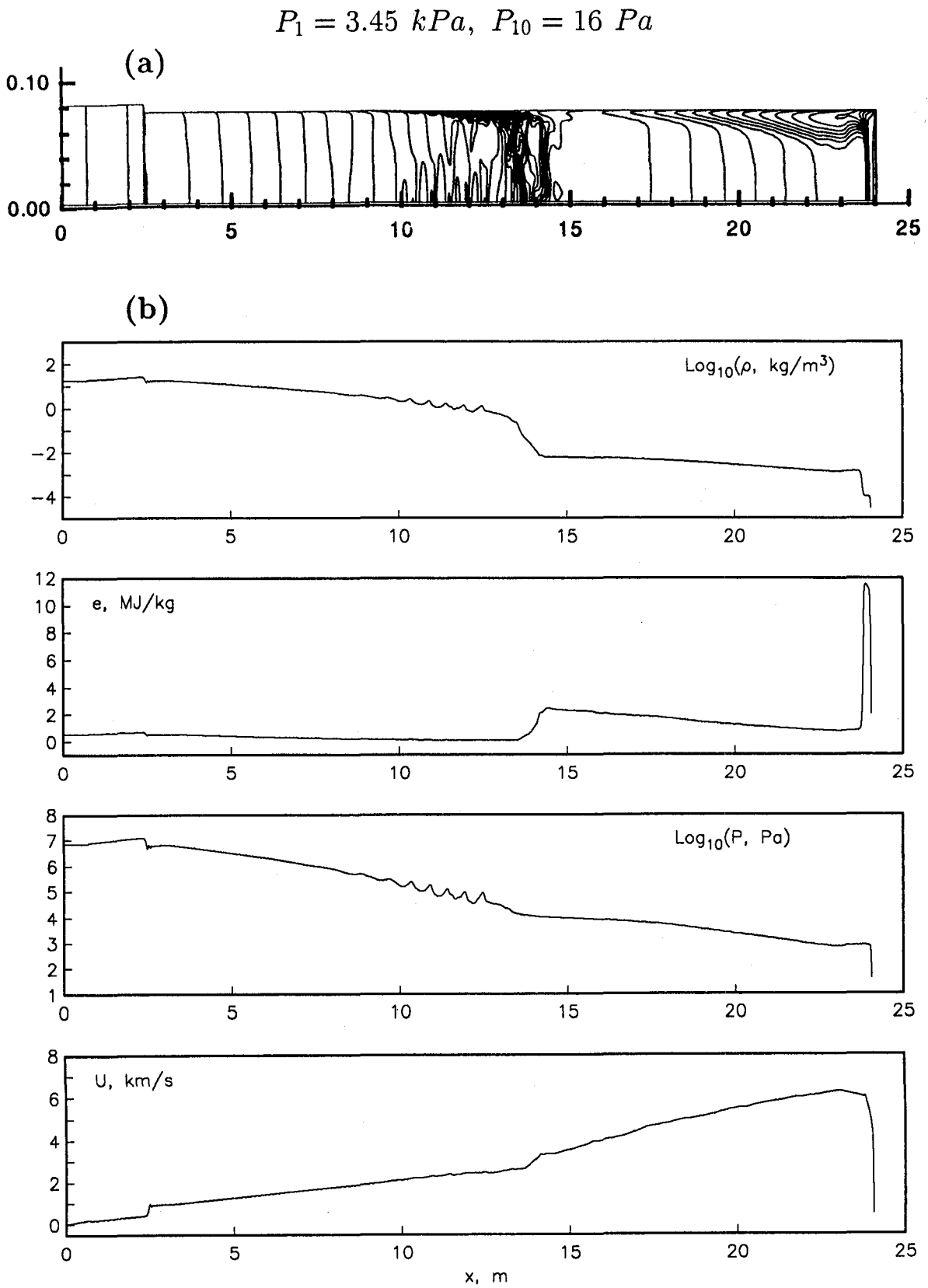

Figure 36: Properties along the axis at $t = 4.4\ ms$ for case 1a: (a) density contours; (b) other properties as labelled.

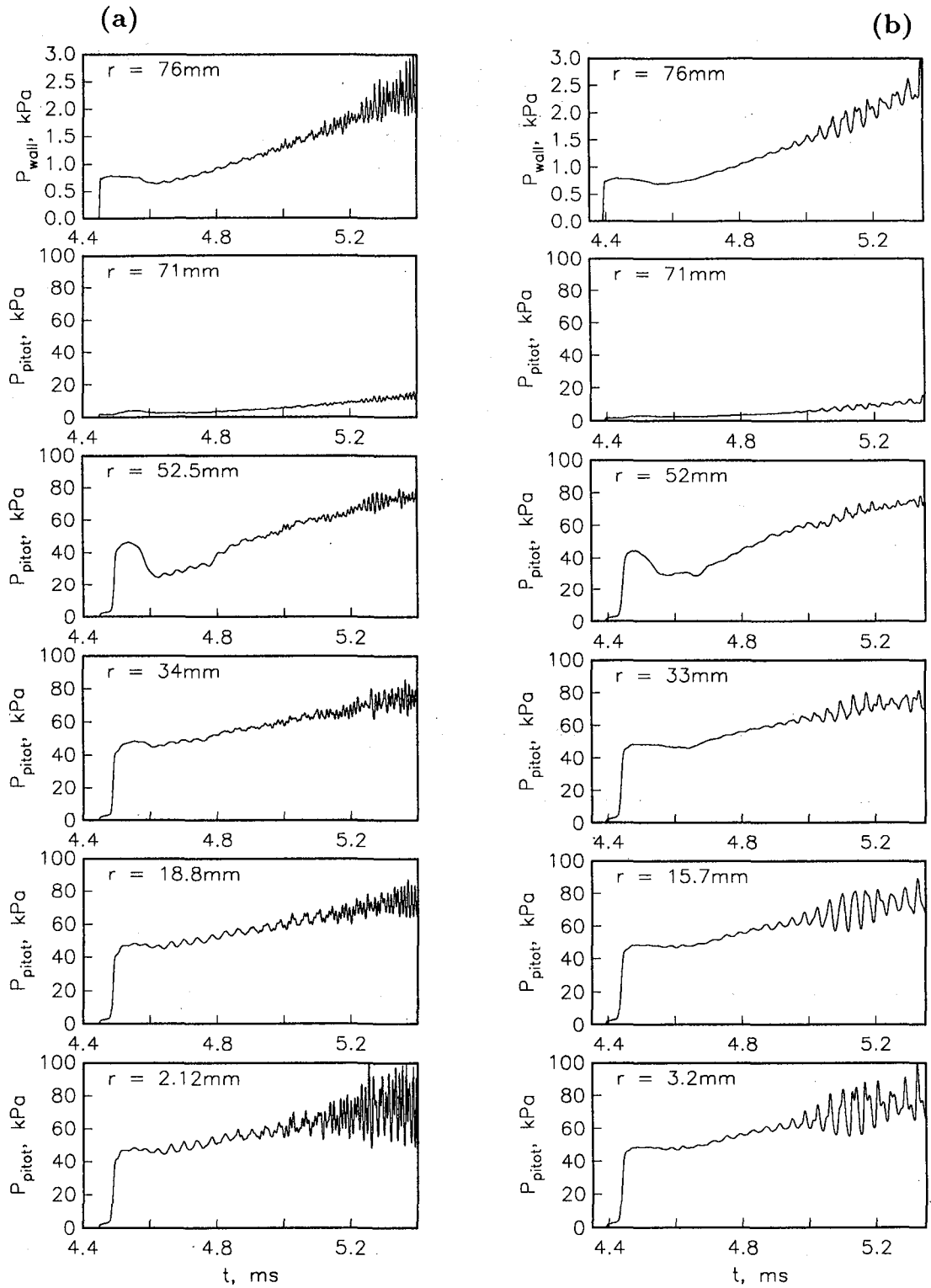

Figure 37: Comparison of Pitot histories at $x = 24\ m$ for (a) 2406×30 grid and (b) 1604×20 grid.

REPORT DOCUMENTATION PAGE

Form Approved
OMB No. 0704-0188

1. AGENCY USE ONLY (Leave blank)	2. REPORT DATE	3. REPORT TYPE AND DATES COVERED
	January 1992	Contractor Report

4. TITLE AND SUBTITLE
NUMERICAL SIMULATION OF TRANSIENT HYPERVELOCITY FLOW IN AN EXPANSION TUBE

5. FUNDING NUMBERS
C NAS1-18605
WU 505-90-52-01

6. AUTHOR(S)
P. A. Jacobs

7. PERFORMING ORGANIZATION NAME(S) AND ADDRESS(ES)
Institute for Computer Applications in Science and Engineering
Mail Stop 132C, NASA Langley Research Center
Hampton, VA 23665-5225

8. PERFORMING ORGANIZATION REPORT NUMBER
ICASE Interim Report 20

9. SPONSORING/MONITORING AGENCY NAME(S) AND ADDRESS(ES)
National Aeronautics and Space Administration
Langley Research Center
Hampton, VA 23665-5225

10. SPONSORING/MONITORING AGENCY REPORT NUMBER
NASA CR-189601
ICASE Interim Report 20

11. SUPPLEMENTARY NOTES
Langley Technical Monitor: Michael F. Card
Final Report

12a. DISTRIBUTION/AVAILABILITY STATEMENT
Unclassified - Unlimited

Subject Category 34, 09

12b. DISTRIBUTION CODE

13. ABSTRACT (Maximum 200 words)

We present several numerical simulations of the transient flow of helium in an expansion tube. The aim of the exercise is to provide further information on (and hopefully further insight into) the operational problems of the NASA Langley expansion tube. The calculations were performed with an axisymmetric Navier-Stokes code based on a finite-volume formulation and upwinding techniques. Although laminar flow and ideal bursting of the diaphragms was assumed, the simulations showed some of the important features seen in the experiments. In particular, the discontinuity in tube diameter at the primary diaphragm station introduced a transverse perturbation to the expanding driver gas and this perturbation was seen to propagate into the test gas under some flow conditions. The disturbances seen in the test flow can be characterized as either "small-amplitude" noise possibly introduced during shock compression or "large-amplitude" noise associated with the passage of the reflected head of the unsteady expansion.

14. SUBJECT TERMS	15. NUMBER OF PAGES
expansion tube; numerical simulation	58
	16. PRICE CODE A04

17. SECURITY CLASSIFICATION OF REPORT	18. SECURITY CLASSIFICATION OF THIS PAGE	19. SECURITY CLASSIFICATION OF ABSTRACT	20. LIMITATION OF ABSTRACT
Unclassified	Unclassified		

NSN 7540-01-280-5500

Standard Form 298 (Rev. 2-89)
Prescribed by ANSI Std Z39-18
298-102

NASA-Langley, 1992